International Journal of Nanomedicine

Dovepress
Taylor & Francis Group

Open Access Full Text Article

ORIGINAL RESEARCH

Bioactive Nanocomposite-Mediated Macrophage Metabolic Shift Orchestrates Pro-Regenerative Healing in the Diabetic Wound Microenvironment

Tianding Shen[1,*], Xiaowei Xu[2,*], Zhenhe Guo[3,*], Wangmei Zhou[4,*], Xiuyun Xiao[1], Shunxin Liao[5], Jiejun Huang[6], Xiaoyan Liu[7], Zhexiang Fan[1]

[1]Department of Plastic and Aesthetic Surgery, Nanfang Hospital, Southern Medical University, Guangzhou, Guangdong, 510515, People's Republic of China; [2]School of Second Clinical Medicine, Southern Medical University, Guangzhou, Guangdong, 510515, People's Republic of China; [3]Department of Plastic and Aesthetic Surgery, The Third Affiliated Hospital of Southern Medical University, Guangzhou, Guangdong, 510630, People's Republic of China; [4]Medical Imaging Center, Nanfang Hospital, Southern Medical University, Guangzhou, Guangdong, 510515, People's Republic of China; [5]Jiujiang City Key Laboratory of Cell Therapy, Department of Plastic and Cosmetic Surgery, JiuJiang NO.1 People's Hospital, Jiujiang, Jiangxi, 332000, People's Republic of China; [6]Department of Production and Research Development, Guangdong SEMYTAI Biotechnology Co., Ltd, Zhuhai, Guangdong, 519080, People's Republic of China; [7]Department of Hematology, Sun Yat-sen Memorial Hospital, Sun Yat-sen University, Guangzhou, Guangdong, 510120, People's Republic of China

*These authors contributed equally to this work

Correspondence: Xiaoyan Liu; Zhexiang Fan, Email liuxy233@mail.sysu.edu.cn; zhexiang1990@smu.edu.cn

Introduction: Chronic diabetic wounds suffer from persistent oxidative stress, unresolved inflammation, and impaired neovascularization, with limited effective therapies.

Methods: We developed a biomimetic nanocomposite (PEG-HS/TiO_2) combining antioxidant TiO_2 with sustained-release honeysuckle. In vitro, we evaluated ROS scavenging, cellular senescence, VEGF expression, and macrophage polarization. In vivo, we assessed wound closure, neovascularization, collagen remodeling, and inflammatory markers in a diabetic mouse model.

Results: PEG-HS/TiO_2 achieved sustained HS release over 72 hours. It scavenged superoxide and H_2O_2, reduced endothelial ROS by approximately 89%, suppressed senescence markers, and restored VEGF expression (>7-fold increase vs. H_2O_2 control). The nanocomposite shifted macrophages from M1 to M2 phenotype, increasing the CD206/CD86 ratio. In vivo, PEG-HS/TiO_2 accelerated wound closure (76% wound area reduction by day 7 vs. 18% in Sham), enhanced CD31+ vessels (6.3-fold vs. Sham), improved collagen organization, reduced M1 macrophages by 85% and IL-1β by 73%, increased IL-10 by 3.1-fold, and lowered systemic CRP and PCT.

Discussion: PEG-HS/TiO_2 breaks the diabetic wound pathology cycle through ROS neutralization, anti-senescence, and macrophage immunometabolic reprogramming, representing a promising strategy for diabetic wound management.

Keywords: diabetic wound healing, nanozyme, reactive oxygen species, macrophage polarization, immunometabolic reprogramming, honeysuckle

Introduction

Chronic diabetic wounds, including diabetic foot ulcers, represent one of the most debilitating complications of diabetes mellitus, affecting approximately 15–25% of diabetic patients over their lifetime.[1] These non-healing wounds are characterized by a protracted inflammatory phase, impaired angiogenesis and defective extracellular matrix (ECM) remodeling, frequently culminating in lower-extremity amputation and significant morbidity.[2] Despite advances in standard-of-care interventions—including surgical debridement, offloading, infection control, and revascularization[3]—the clinical management of diabetic wounds remains suboptimal, with recurrence rates approaching 40% within one year of healing.[4] This therapeutic shortfall underscores an urgent need for novel strategies that target the fundamental pathophysiological drivers underlying impaired tissue repair in the diabetic milieu.

https://doi.org/10.2147/IJN.S617254
Received: 21 April 2026
Accepted: 20 June 2026
Published: 30 June 2026

A central pathological hallmark of the diabetic wound microenvironment is the profound dysregulation of redox homeostasis. Persistent hyperglycemia promotes the overproduction of reactive oxygen species (ROS) via multiple pathways, including mitochondrial electron transport chain leakage, NADPH oxidase activation, and advanced glycation end-product (AGE) formation.[5,6] Excessive ROS accumulation not only inflicts direct oxidative damage upon resident cells and ECM components but also serves as a critical signaling node that perpetuates a self-amplifying cycle of inflammation and cellular senescence.[7] Specifically, elevated ROS levels stabilize hypoxia-inducible factor 1-alpha (HIF-1α),[8,9] driving a pro-glycolytic metabolic shift in macrophages that reinforces a pro-inflammatory (M1) phenotype and impairs the phenotypic transition to a pro-regenerative (M2) state essential for resolution of inflammation and initiation of tissue repair.[10,11] Concomitantly, oxidative stress precipitates premature senescence in endothelial cells and fibroblasts, compromising their proliferative and angiogenic capacities and further stalling the healing cascade.[12,13] Therefore, therapeutic interventions capable of concurrently restoring redox equilibrium and reprogramming maladaptive immune responses may hold considerable promise for disrupting the pathological cycle of chronic diabetic wounds.

The application of nanotechnology in wound healing has witnessed rapid progress in recent years, with various nanomaterial-based platforms—including polymeric nanoparticles, lipid nanoparticles, metal-based nanoparticles, and exosome-based systems—being developed to address the multifaceted challenges of diabetic wound repair.[14] Among these, surface-functionalized nanocomposites that combine catalytic ROS-scavenging activity with sustained release of bioactive phytochemicals represent a particularly promising yet underexplored approach. Nanomaterials endowed with intrinsic enzyme-mimetic activities—often termed nanozymes—have emerged as attractive candidates for antioxidant therapy owing to their robust stability, tunable catalytic properties, and capacity for sustained ROS neutralization.[15,16] Titanium dioxide (TiO_2) nanoparticles have garnered particular attention for their ability to mimic the catalytic functions of superoxide dismutase (SOD) and catalase (CAT), thereby facilitating the sequential dismutation of superoxide anions (O_2^-) to hydrogen peroxide (H_2O_2) and the subsequent decomposition of H_2O_2 to water and molecular oxygen.[17,18] However, the therapeutic translation of bare TiO_2 nanomaterials is frequently hampered by suboptimal colloidal stability, potential dose-dependent cytotoxicity, and a lack of tissue-specific bioactivity.[19,20] Surface functionalization with hydrophilic polymers such as polyethylene glycol (PEG) has been shown to improve aqueous dispersibility and mitigate nonspecific protein adsorption, thereby enhancing biocompatibility.[21,22] Nevertheless, strategies that merely attenuate oxidative stress may prove insufficient to fully resolve the complex inflammatory and metabolic derangements characteristic of the diabetic wound.[23]

An emerging paradigm in wound therapeutics involves the integration of inorganic catalytic cores with naturally derived bioactive phytochemicals to achieve multifaceted modulation of the healing microenvironment.[24,25] Honeysuckle (Lonicera japonica), a widely utilized medicinal herb in traditional Chinese medicine, is rich in chlorogenic acid, luteolin, and other polyphenolic constituents possessing documented anti-inflammatory, antioxidant, and antimicrobial properties.[26,27] The sustained release of such phytochemicals from a nanocarrier platform may synergize with nanozyme-mediated ROS scavenging to simultaneously address oxidative injury and immune dysregulation. Despite the theoretical appeal of such hybrid constructs, systematic investigations examining their capacity to reprogram immunometabolic flux and promote regenerative healing in diabetic wounds remain limited.

In the present study, we report the development and comprehensive evaluation of a biomimetic nanocomposite platform, PEG-HS/TiO_2, which integrates the intrinsic SOD- and CAT-mimetic activities of mesoporous anatase TiO_2 with the sustained-release bioactivity of honeysuckle (HS)-derived phytochemicals. We hypothesize that this integrated design will concurrently neutralize pathological ROS burdens, alleviate oxidative stress-induced cellular senescence, and redirect macrophage polarization toward a pro-regenerative M2 phenotype through redox-dependent metabolic reprogramming.

The research focus of this study is to elucidate how PEG-HS/TiO_2 orchestrates pro-regenerative healing in diabetic wounds through macrophage immunometabolic reprogramming. The key challenges addressed include: (1) persistent oxidative stress and chronic M1-dominant inflammation in the diabetic wound microenvironment; (2) impaired angiogenesis due to endothelial senescence; (3) lack of direct evidence for chemical integration of HS with the nanocomposite; and (4) incomplete biosafety assessment of topical nanomaterial application. By systematically characterizing the physicochemical properties, antioxidant activity, cellular effects, in vivo wound healing efficacy, and biosafety of PEG-

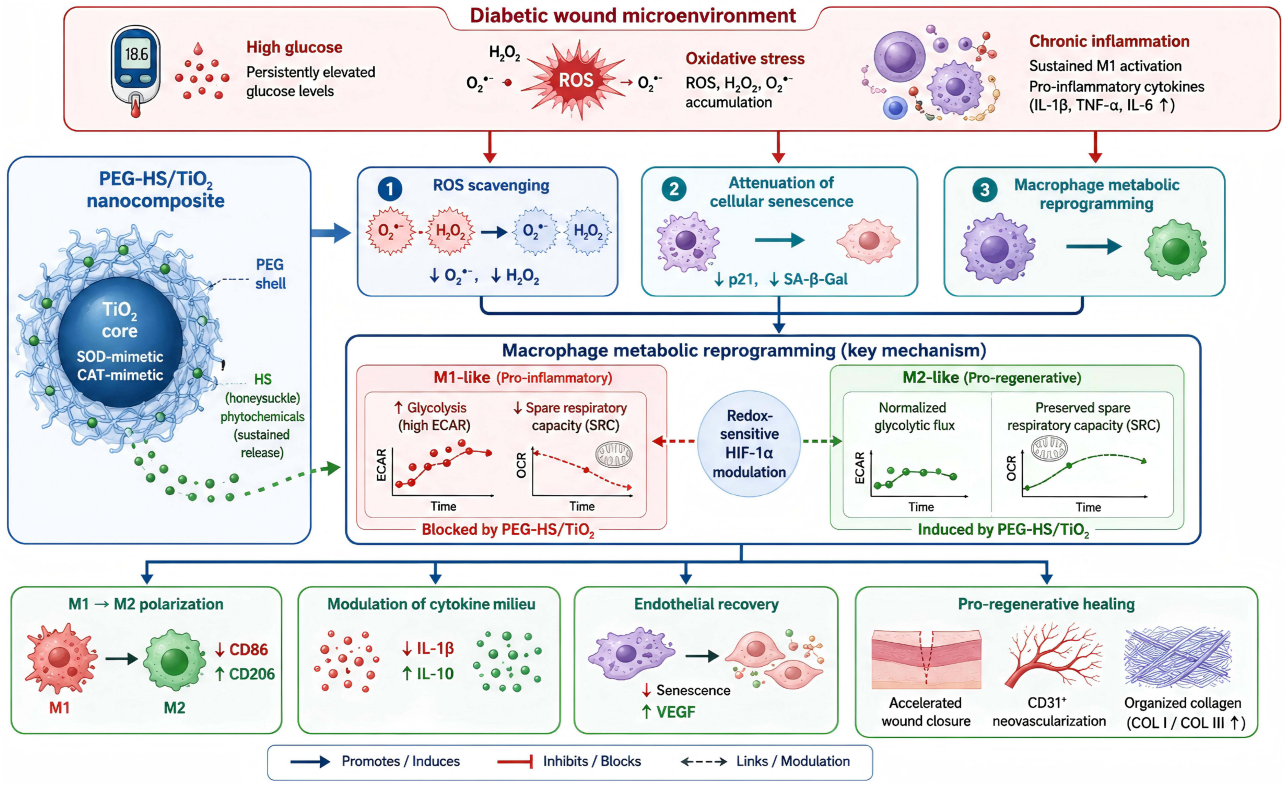

Scheme 1 Schematic illustration of the therapeutic mechanism of PEG-HS/TiO_2 nanocomposites for diabetic wound healing. Downward arrows (↓) indicate a decrease or suppression, while upward arrows (↑) indicate an increase or enhancement of the respective parameters.

HS/TiO_2, we aim to provide a comprehensive mechanistic rationale for this nanocomposite as a promising strategy for diabetic wound management."

To test this hypothesis, we systematically characterized the physicochemical properties of PEG-HS/TiO_2, assessed its antioxidant efficacy and cytocompatibility in vitro, and delineated its effects on endothelial cell senescence and macrophage immunometabolism. The therapeutic potential of the nanocomposite was subsequently evaluated in a diabetic murine model of full-thickness excisional wound healing, with particular attention to wound closure kinetics, neovascularization, local and systemic inflammatory modulation, and long-term tissue remodeling quality (Scheme 1). Our findings provide a mechanistic rationale for the application of bioactive nanocomposites that leverage both inorganic catalysis and natural phytochemistry to orchestrate pro-regenerative healing in the challenging diabetic wound microenvironment.

Materials and Methods

Materials and Reagents

Titanium dioxide precursors, polyethylene glycol (PEG, Mw ~2000 Da), and analytical grade organic solvents were procured from Sigma-Aldrich (St. Louis, MO, USA). Honeysuckle (Lonicera japonica) extract (HS) was supplied by Xi'an Rongsheng Biotechnology Co., Ltd. (Xi'an, China). Hydrogen peroxide (H_2O_2, 30% w/w), xanthine, xanthine oxidase (from bovine milk), and electron paramagnetic resonance (EPR) spin-trapping agents 5,5-dimethyl-1-pyrroline N-oxide (DMPO) and 2,2,6,6-tetramethylpiperidine (TEMP) were obtained from Aladdin Biochemical Technology Co., Ltd. (Shanghai, China). Cell culture media including Dulbecco's Modified Eagle Medium (DMEM), endothelial cell growth medium-2 (EGM-2), fetal bovine serum (FBS), penicillin-streptomycin (10,000 U/mL), and trypsin-EDTA (0.25%) were purchased from Gibco (Thermo Fisher Scientific, Waltham, MA, USA). Cell Counting Kit-8 (CCK-8), Hydrogen Peroxide Assay Kit, Superoxide Dismutase Assay Kit (WST-1 method), Senescence-Associated β-Galactosidase (SA-β-Gal) Staining Kit, and MitoSOX Red mitochondrial superoxide indicator were acquired from

https://doi.org/10.2147/IJN.S617254

Beyotime Biotechnology (Shanghai, China). 2',7'-Dichlorodihydrofluorescein diacetate (DCFH-DA) was obtained from Sigma-Aldrich. TRIzol reagent, PrimeScript RT Reagent Kit, and SYBR Green Master Mix were sourced from Takara Bio (Kusatsu, Shiga, Japan). Primary and secondary antibodies used for immunofluorescence staining are detailed in the respective subsections below. Ultrapure deionized water (resistivity 18.2 MΩ·cm) was generated using a Milli-Q Reference water purification system (Merck Millipore, Billerica, MA, USA) and employed throughout all experimental procedures.

Synthesis of PEG-HS/TiO_2 Nanocomposites

PEG-HS/TiO_2 nanocomposites were synthesized via a sol-gel methodology followed by sequential surface PEGylation and honeysuckle (HS) loading (Figure 1A).

Synthesis of Mesoporous Anatase TiO_2

Titanium tetraisopropoxide (TTIP, 98%, Sigma-Aldrich, St. Louis, MO, USA) was used as the titanium precursor. In a typical procedure, 2.95 mL (10 mmol) of TTIP was dissolved in 30 mL of absolute ethanol under vigorous magnetic stirring at room temperature. Separately, 1.0 g of Pluronic P123 ($EO_{20}PO_{70}EO_{20}$, Mw ≈ 5800, Sigma-Aldrich) was dissolved in 20 mL of deionized water containing 1.0 mL of glacial acetic acid (pH adjusted to 4.5). The TTIP/ethanol solution was then added dropwise to the P123-containing solution under continuous stirring at 40 °C. The resulting mixture was stirred for 24 h at 40 °C to allow complete hydrolysis and condensation. The obtained white precipitate was collected by centrifugation (12,000 rpm, 15 min), washed three times with deionized water and twice with absolute ethanol, and then dried at 60 °C for 12 h. The dried powder was calcined in a muffle furnace at 450 °C for 4 h (ramp rate 2 °C/min) to remove the structure-directing agent and obtain mesoporous anatase TiO_2.

PEGylation of TiO_2

To improve aqueous dispersibility and colloidal stability, the synthesized TiO_2 nanoparticles were surface-modified with polyethylene glycol (PEG, Mw ≈ 2000 Da, Sigma-Aldrich) via covalent conjugation. Briefly, 200 mg of TiO_2 nanoparticles were dispersed in 50 mL of anhydrous ethanol by ultrasonication for 30 min. Subsequently, 10 mg (5% w/w relative to TiO_2) of succinimidyl carbonate–PEG–silane (SC-PEG-silane, Nanocs Inc., Boston, MA, USA) was added to the dispersion. The reaction mixture was stirred at 60 °C for 12 h under a nitrogen atmosphere. The PEGylated TiO_2 (PEG-TiO_2) was collected by centrifugation (12,000 rpm, 10 min), washed three times with anhydrous ethanol to remove unreacted PEG, and dried under vacuum at 40 °C for 24 h.

Honeysuckle (HS) Loading

Honeysuckle extract (Lonicera japonica, Xi'an Rongsheng Biotechnology Co., Ltd., Xi'an, China) was dissolved in deionized water to prepare a stock solution of 5 mg/mL (calculated as chlorogenic acid equivalents). For HS loading, 100 mg of PEG-TiO_2 was dispersed in 50 mL of HS aqueous solution (2 mg/mL) by ultrasonication for 10 min. The mixture was stirred at room temperature for 24 h in the dark to allow physical adsorption and electrostatic interaction between the HS phytochemicals and the PEGylated TiO_2 surface. After loading, the PEG-HS/TiO_2 nanocomposites were collected by centrifugation (12,000 rpm, 10 min), washed twice with deionized water to remove surface-adsorbed but unbound HS, and lyophilized using a freeze dryer (Labconco FreeZone, Kansas City, MO, USA). The lyophilized powder was stored at 4 °C under desiccated conditions until further use.

Quantification of HS Loading and Encapsulation Efficiency

Quantification of HS loading by UV-Vis spectrophotometry: a standard curve of chlorogenic acid (the main active component of HS) was constructed at 327 nm (R^2 = 0.999). The supernatant and washing solutions collected during $nCeO_2$@HS preparation were combined, and the unloaded HS concentration was determined. DLC was calculated using the following formulas:

DLC (%) = (Weight of HS in nanocomposites / Weight of nanocomposites) × 100%,where A_0 is the absorbance of control and A_1 is the absorbance of the sample.

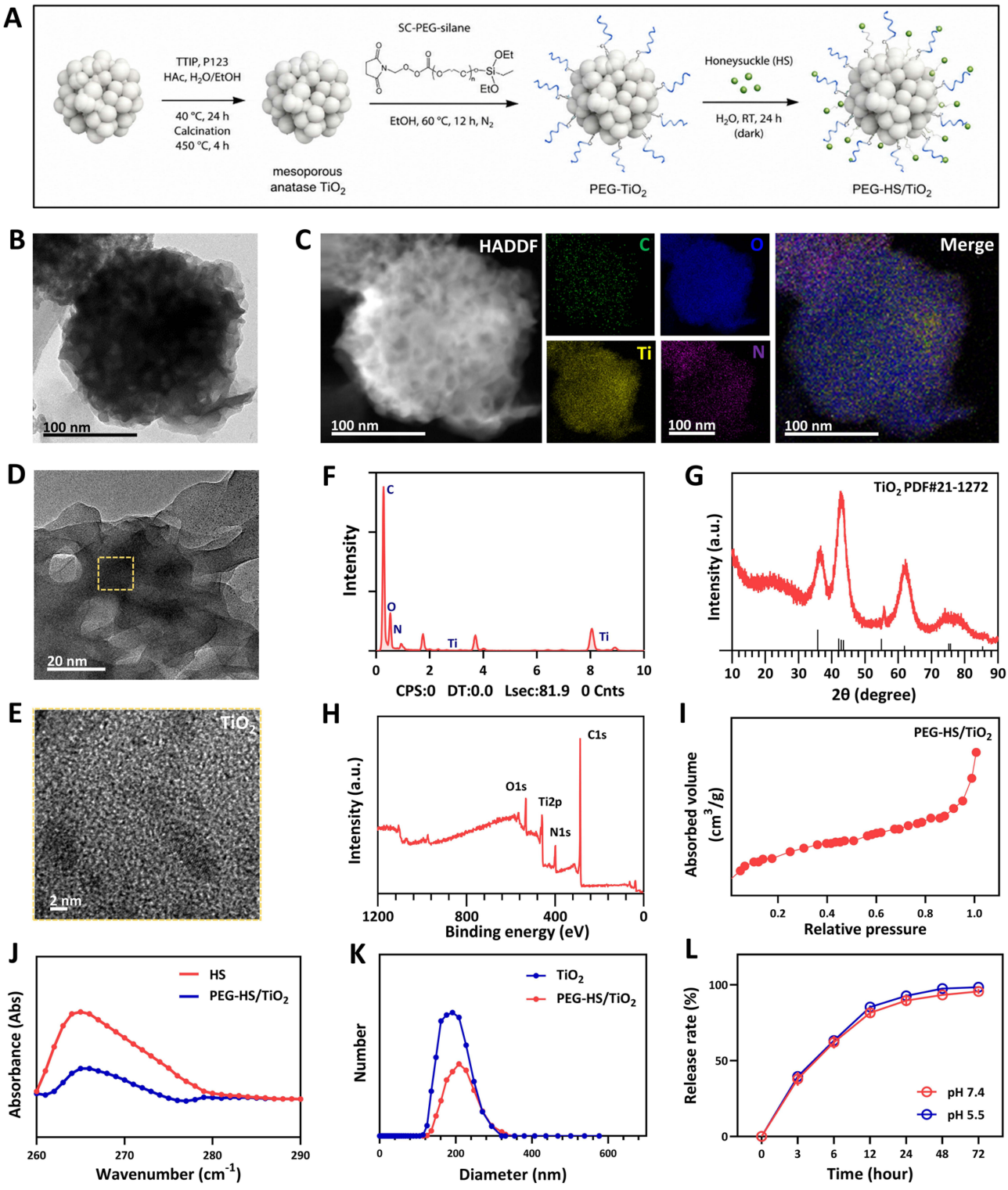

Figure 1 Characterization of PEG-HS/TiO_2 nanocomposites. (**A**) Illustration of the PEG-HS/TiO_2 synthesis procedure. (**B**–**C**) HRTEM image and EDS elemental mapping of PEG-HS/TiO_2. (**D**–**E**) AC HAADF-STEM image of PEG-HS/TiO_2. (**F**) Intensity of elements. (**G**) XRD patterns of PEG-HS/TiO_2. The enlarged area within the yellow dashed box in Figure 1f is shown in Figure 1e. (**H**) XPS profiles of PEG-HS/TiO_2. (**I**) Nitrogen adsorption-desorption isotherms. (**J**) Ultraviolet–visible (UV–Vis) spectral comparisons of honeysuckle (HS) and PEG-HS/TiO_2. (**K**) DLS analysis of particle size for HS and PEG-HS/TiO_2. (**L**) HS release rate of PEG-HS/TiO_2 at different pH levels by UV–Vis. n=3, error bars indicate the mean ± standard deviation.

https://doi.org/10.2147/IJN.S617254

Physicochemical Characterization

Transmission Electron Microscopy (TEM)

The morphology and microstructure of PEG-HS/TiO_2 were examined using a JEOL JEM-2100F field-emission transmission electron microscope (JEOL Ltd., Akishima, Tokyo, Japan) operated at an accelerating voltage of 200 kV. High-resolution TEM (HRTEM) images were acquired on the same instrument. Aberration-corrected high-angle annular dark-field scanning TEM (AC HAADF-STEM) imaging was performed on a Titan Themis Z instrument (Thermo Fisher Scientific, Waltham, MA, USA) equipped with a probe corrector. Energy-dispersiv e X-ray spectroscopy (EDS) elemental mapping was conducted using an Oxford Instruments X-Max*N* 80T detector (Oxford Instruments, Abingdon, UK) coupled to the TEM system.

X-Ray Diffraction (XRD)

XRD patterns were recorded on a Rigaku SmartLab X-ray diffractometer (Rigaku Corporation, Akishima, Tokyo, Japan) employing Cu Kα radiation (λ = 1.5406 Å). Data were collected over a 2θ range of 10° to 80° with a step size of 0.02° and a scan rate of 2° min^{-1}. The operating voltage and current were set at 40 kV and 40 mA, respectively.

X-Ray Photoelectron Spectroscopy (XPS)

XPS analysis was carried out using a Thermo Scientific K-Alpha X-ray photoelectron spectrometer (Thermo Fisher Scientific, Waltham, MA, USA) equipped with a monochromatic Al Kα X-ray source (hν = 1486.6 eV). Survey spectra were acquired at a pass energy of 200 eV, while high-resolution regional spectra were collected at a pass energy of 50 eV. Binding energies were calibrated relative to the adventitious C 1s peak at 284.8 eV.

Nitrogen Adsorption-Desorption Isotherms

Textural properties were evaluated by nitrogen physisorption at 77 K using a Micromeritics ASAP 2460 surface area and porosimetry analyzer (Micromeritics Instrument Corporation, Norcross, GA, USA). Prior to measurement, samples were degassed under vacuum at 120 °C for 6 h. The specific surface area was calculated using the Brunauer-Emmett-Teller (BET) method over a relative pressure (P/P_0) range of 0.05–0.30. Pore size distribution was derived from the adsorption branch of the isotherm using the Barrett-Joyner-Halenda (BJH) model.

Ultraviolet-Visible (UV-Vis) Spectroscopy

UV-Vis absorption spectra were acquired on a Shimadzu UV-2600 spectrophotometer (Shimadzu Corporation, Kyoto, Japan) equipped with a tungsten-halogen and deuterium light source. Spectra were recorded over the wavelength range of 200–800 nm using quartz cuvettes with a 1 cm path length.

Dynamic Light Scattering (DLS)

Hydrodynamic diameter and size distribution were measured using a Malvern Zetasizer Nano ZS instrument (Malvern Panalytical, Malvern, Worcestershire, UK) equipped with a 4 mW He-Ne laser (λ = 633 nm) and operating at a detection angle of 173° (backscatter mode). Measurements were performed at 25 °C following equilibration for 120 s. Each sample was measured in triplicate, with each measurement consisting of 12–15 runs.

Zeta Potential Measurement

Zeta potentials of TiO_2, PEG-TiO_2, and PEG-HS/TiO_2 were measured using a Malvern Zetasizer Nano ZS instrument (Malvern Panalytical, Malvern, UK). Samples were dispersed in deionized water (pH 7.4) at a concentration of 0.1 mg/mL and sonicated for 10 min prior to measurement. All measurements were performed at 25 °C with automatic attenuation and voltage selection. Each sample was measured in triplicate, and the results are reported as mean ± standard deviation (SD).

In vitro HS Release Profile

The release kinetics of HS from PEG-HS/TiO_2 were evaluated in phosphate-buffered saline (PBS) at pH 5.5 and pH 7.4 at 37 °C. At predetermined time points (0, 3, 6, 12, 24, 48, and 72 h), aliquots of the release medium were withdrawn and replaced with an equal volume of fresh pre-warmed PBS. The concentration of released HS was quantified by UV-Vis

spectrophotometry at the characteristic absorption wavelength (λ_max = 327 nm, as determined by full-wavelength scanning of HS extract), with reference to a standard calibration curve constructed from known concentrations of HS extract ($R^2 > 0.999$). The selection of these pH conditions was based on the following considerations: pH 7.4 represents the physiological pH of normal skin and healing wounds, serving as a control condition. pH 5.5 was chosen to mimic the mildly acidic microenvironment characteristic of chronic, non-healing diabetic wounds. Although normal acute wounds exhibit an initial acidic pH (~5.5–6.5) that gradually shifts toward neutrality during healing, diabetic wounds are often characterized by persistently elevated pH (ranging from 7.2 to 8.5) due to factors such as bacterial colonization, impaired perfusion, and chronic inflammation. However, during the initial inflammatory phase or in wounds colonized by certain bacteria, localized acidic microenvironments can also occur. Therefore, pH 5.5 was included to evaluate HS release under conditions of mild acidity that may be encountered during the early inflammatory stage, while pH 7.4 represents the later healing phase or non-healing alkaline environment. This dual-pH approach allows us to assess the robustness of the sustained-release platform across different pathological states. The concentration of released HS was quantified by UV-Vis spectrophotometry at the characteristic absorption wavelength (λ_max = 327 nm, as determined by full-wavelength scanning of HS extract). The HS loading content in PEG-HS/TiO_2 was calculated as: *(amount of HS loaded / initial amount of HS added) × 100%*, and the equivalent HS concentration used in subsequent in vivo experiments was normalized accordingly.

Release Kinetics Modeling

The cumulative release data were fitted to zero-order ($Q = k_0 \cdot t$), first-order ($\ln(1-Q/Q_{max}) = -k_1 \cdot t$), and Higuchi ($Q = k\_H \cdot t^{1/2}$) kinetic models. The Korsmeyer-Peppas model ($\log(Q/Q_{max}) = \log k + n \log t$) was used to evaluate the release mechanism, where $n \leq 0.45$ indicates Fickian diffusion, $0.45 < n < 0.89$ indicates anomalous (non-Fickian) transport, and $n \geq 0.89$ indicates case-II transport (polymer relaxation).

Fourier-Transform Infrared Spectroscopy (FTIR)

FTIR spectra were recorded on a Nicolet iS50 FTIR spectrometer (Thermo Fisher Scientific, Waltham, MA, USA) using the KBr pellet method. Spectra were collected in the range of 400–4000 cm^{-1} with a resolution of 4 cm^{-1} and 32 scans per sample. The characteristic peaks of pure HS, PEG-TiO_2, and PEG-HS/TiO_2 were analyzed to identify shifts indicative of chemical interactions (eg., hydrogen bonding) between HS and the PEGylated TiO_2 surface. A physical mixture of HS and PEG-TiO_2 was also measured as a control to distinguish simple adsorption from chemical binding.

Thermogravimetric Analysis (TGA)

TGA was performed using a TGA 550 thermogravimetric analyzer (TA Instruments, New Castle, DE, USA). Approximately 5–10 mg of each sample (pure HS, PEG-TiO_2, and PEG-HS/TiO_2) was heated from 25 °C to 800 °C at a ramp rate of 10 °C/min under nitrogen atmosphere (flow rate 40 mL/min). The weight loss curves were recorded, and the HS loading content was calculated from the thermal decomposition weight loss difference between PEG-HS/TiO_2 and PEG-TiO_2 in the temperature range corresponding to HS decomposition (200–500 °C).

Evaluation of Antioxidant Activity

Electron Paramagnetic Resonance (EPR) Spectroscopy

The superoxide anion (O_2^-) and hydrogen peroxide (H_2O_2) scavenging capacities of PEG-HS/TiO_2 were assessed using a Bruker EMXplus X-band EPR spectrometer (Bruker BioSpin GmbH, Rheinstetten, Germany) operating at a microwave frequency of approximately 9.8 GHz. For O_2^- detection, the xanthine (0.5 mM)/xanthine oxidase (0.05 U/mL) system was employed as a superoxide-generating source in the presence of the spin trap DMPO (100 mM) in PBS (pH 7.4). For H_2O_2 detection, the spin trapping agent TEMP (50 mM) was utilized. Spectra were recorded at room temperature before and 10 min after the addition of PEG-HS/TiO_2 (100 μg/mL). The following instrument parameters were employed: microwave power, 20 mW; modulation amplitude, 1.0 G; sweep width, 100 G; sweep time, 60s; and time constant, 40.96 ms. Signal attenuation was quantified by peak-to-peak amplitude measurement relative to untreated control samples.

Hydrogen Peroxide Elimination Assay

H_2O_2 elimination was quantified using a commercial Hydrogen Peroxide Assay Kit (Beyotime Biotechnology, Shanghai, China) according to the manufacturer's protocol. Briefly, PEG-HS/TiO_2 (100 μg/mL) was incubated with H_2O_2 (100 μM) in PBS (pH 7.4) at 37 °C for 10 min. Following incubation, the residual H_2O_2 concentration was determined colorimetrically by measuring absorbance at 560 nm using a Thermo Fisher Multiskan FC microplate reader (Thermo Fisher Scientific, Waltham, MA, USA).

Superoxide Dismutase (SOD) Mimetic Activity Assay

Superoxide anion scavenging activity was evaluated using a Superoxide Dismutase Assay Kit based on the WST-1 method (Beyotime Biotechnology, Shanghai, China), following the manufacturer's instructions. Absorbance was measured at 450 nm using the same microplate reader described above. The SOD-mimetic activity was expressed as the percentage inhibition of WST-1 formazan formation relative to the enzyme-free control.

Cell Culture and Cytocompatibility Assessment

Cell Lines and Culture Conditions

Human immortalized keratinocytes (HaCaT), human umbilical vein endothelial cells (HUVEC), and murine fibroblasts (L929) were obtained from the American Type Culture Collection (ATCC, Manassas, VA, USA). HaCaT and L929 cells were cultured in Dulbecco's Modified Eagle Medium (DMEM; Gibco, Thermo Fisher Scientific, Waltham, MA, USA) supplemented with 10% (v/v) heat-inactivated fetal bovine serum (FBS; Gibco) and 1% (v/v) penicillin-streptomycin (10,000 U/mL; Gibco). HUVECs were maintained in endothelial cell growth medium-2 (EGM-2; Lonza, Basel, Switzerland) containing the EGM-2 SingleQuots Supplement Pack (Lonza). All cells were incubated at 37 °C in a humidified atmosphere containing 5% CO_2 using a Thermo Scientific Heracell VIOS 160i CO_2 incubator (Thermo Fisher Scientific).

MTT Assay

Cytocompatibility was evaluated using the MTT assay. Cells were seeded in 96-well plates (Corning) at 5×10^3 cells/well and incubated overnight. Fresh medium containing PEG-HS/TiO_2 (0–200 μg/mL) was then added. As a positive toxicity control, cells were treated with 10% dimethyl sulfoxide (DMSO) for 24 h. After 24 h, MTT solution (5 mg/mL; Sigma-Aldrich) was applied for 4 h. Formazan crystals were dissolved in DMSO, and absorbance was measured at 570 nm using a Thermo Fisher Multiskan FC microplate reader. Viability was expressed relative to untreated controls (set as 100%).

Hemocompatibility Assay

Hemolytic activity was assessed using erythrocytes isolated from healthy C57BL/6J mice. Erythrocyte suspensions (2% v/v in PBS) were incubated with PEG-HS/TiO_2 (0–200 μg/mL) for 2 h at 37 °C. Following centrifugation, supernatant absorbance was measured at 540 nm using a Thermo Fisher Multiskan FC microplate reader. PBS and 1% Triton X-100 (Sigma-Aldrich) served as negative (0%) and positive (100%) controls, respectively.

$$Hemolysis\ (\%) = [(A\_sample - A\_PBS) / (A\_Triton - A\_PBS)] \times 100$$

where A_sample, A_PBS, and A_Triton represent the absorbance values of the sample, PBS control, and Triton X-100 control, respectively. A hemolysis ratio below 5% was considered indicative of acceptable hemocompatibility according to ASTM F756-17 guidelines.

Cellular Uptake Studies

Rhodamine B-labeled PEG-HS/TiO_2 was prepared by covalently conjugating rhodamine B isothiocyanate (Sigma-Aldrich) to the nanocomposite surface according to established protocols. HUVECs were seeded onto sterile glass coverslips (Fisherbrand, Thermo Fisher Scientific) placed in 24-well plates at a density of 2×10^4 cells per well and allowed to adhere overnight. Cells were then incubated with rhodamine-labeled PEG-HS/TiO_2 (50 μg/mL) for 3, 12, and 24 h at 37 °C. At each designated time point, cells were washed three times with ice-cold PBS, fixed with 4% (w/v)

paraformaldehyde (Sigma-Aldrich) in PBS for 15 min at room temperature, and permeabilized with 0.1% (v/v) Triton X-100 in PBS for 10 min. Nuclei were counterstained with 4',6-diamidino-2-phenylindole (DAPI; 1 μg/mL; Beyotime Biotechnology) for 5 min. Coverslips were mounted onto glass slides using ProLong Gold Antifade Mountant (Thermo Fisher Scientific). Cellular uptake was visualized using a Leica TCS SP8 confocal laser scanning microscope (CLSM; Leica Microsystems, Wetzlar, Germany) equipped with a 63× oil immersion objective (numerical aperture 1.4). Quantitative analysis of uptake efficiency was performed by flow cytometry using a BD FACSCanto II flow cytometer (Becton Dickinson, Franklin Lakes, NJ, USA). A minimum of 10,000 events were acquired per sample, and data were analyzed using FlowJo software version 10.8 (Tree Star, Ashland, OR, USA).

Oxidative Stress-Induced Cellular Senescence Model

HUVECs were seeded in 6-well plates or on glass coverslips as appropriate and cultured until reaching approximately 70% confluence. To induce oxidative stress and establish a senescent phenotype, cells were exposed to H_2O_2 (200 μM) in serum-free medium for 2 h at 37 °C. Following H_2O_2 challenge, the medium was aspirated, and cells were gently washed twice with PBS. Fresh complete culture medium containing PEG-HS/TiO_2 (100 μg/mL) or an equivalent volume of PBS vehicle control was then added, and cells were incubated for an additional 24 h.

Senescence-Associated β-Galactosidase (SA-β-Gal) Staining

SA-β-Gal activity was detected using a commercial Senescence-Associated β-Galactosidase Staining Kit (Beyotime Biotechnology, Shanghai, China) strictly according to the manufacturer's protocol. Briefly, cells were fixed with the provided fixative solution for 15 min at room temperature, washed with PBS, and incubated with the SA-β-Gal staining solution (containing X-gal) at 37 °C overnight in a CO_2-free incubator. Stained cells were imaged under bright-field illumination using an Olympus IX73 inverted microscope (Olympus Corporation, Tokyo, Japan) equipped with a DP74 digital camera. The percentage of SA-β-Gal-positive cells (blue-stained cells) was quantified from five randomly selected fields per sample using ImageJ software (National Institutes of Health, Bethesda, MD, USA).

Immunofluorescence Staining for p21

Cells grown on coverslips were fixed with 4% paraformaldehyde for 15 min, permeabilized with 0.1% Triton X-100 for 10 min, and blocked with 5% bovine serum albumin (BSA; Sigma-Aldrich) in PBS for 1 h at room temperature. Cells were then incubated with a rabbit anti-p21 primary antibody (1:200 dilution; Abcam, Cambridge, UK) overnight at 4 °C. Following three washes with PBS containing 0.05% Tween-20 (PBST), cells were incubated with an Alexa Fluor 488-conjugated goat anti-rabbit IgG (H+L) secondary antibody (1:500 dilution; Thermo Fisher Scientific) for 1 h at room temperature in the dark. Nuclei were counterstained with DAPI. Images were captured using the Leica TCS SP8 CLSM system described above.

Intracellular and Mitochondrial ROS Detection

Intracellular total ROS and mitochondrial superoxide levels were assessed using the fluorescent probes 2',7'-dichlorodihydrofluorescein diacetate (DCFH-DA) and MitoSOX Red, respectively. HUVECs subjected to the H_2O_2-induced senescence protocol with or without PEG-HS/TiO_2 treatment were incubated with DCFH-DA (10 μM; Sigma-Aldrich) or MitoSOX Red (5 μM; Beyotime Biotechnology) in serum-free medium for 30 min at 37 °C in the dark. Following incubation, cells were washed three times with pre-warmed PBS to remove excess probe. For DCFH-DA-loaded cells, fluorescence images were acquired immediately using the Leica TCS SP8 CLSM with excitation at 488 nm and emission collection at 515–540 nm. For MitoSOX Red-loaded cells, excitation was performed at 514 nm with emission collection at 560–600 nm. Mean fluorescence intensities were quantified using ImageJ software from a minimum of five randomly selected fields per sample across three independent biological replicates.

RNA Extraction and Quantitative Real-Time PCR (qPCR)

Total RNA was extracted using TRIzol reagent (Takara Bio) according to the manufacturer's protocol. RNA concentration and purity were assessed using a NanoDrop One spectrophotometer (Thermo Fisher Scientific). cDNA was

Table 1 Primer Sequences Used for Quantitative Real-Time PCR

Gene	Forward Primer (5' → 3')	Reverse Primer (5' → 3')
VEGF	AGGCTGCTGTAACGATGAAG	TCTCCTATGTGCTGGCTTTG
IL-1β	GCAACTGTTCCTGAACTCAACT	ATCTTTTGGGGTCCGTCAACT
IL-6	TAGTCCTTCCTACCCCAATTTCC	TTGGTCCTTAGCCACTCCTTC
IFN-γ	ATGAACGCTACACACTGCATC	CCATCCTTTTGCCAGTTCCTC
IL-10	GCTCTTACTGACTGGCATGAG	CGCAGCTCTAGGAGCATGTG
GAPDH	AGGTCGGTGTGAACGGATTTG	TGTAGACCATGTAGTTGAGGTCA
LDHA	TGTCTCCAGCAAAGACTACTGT	GACTGTACTTGACAATGTTGGGA
PDK1	GGACTTCGGGTCAGTGAATGC	TCCTGAGAAGATTGTCGGGGA

synthesized from 1 μg of total RNA using the PrimeScript RT Reagent Kit with gDNA Eraser (Takara Bio). qPCR was performed on an Applied Biosystems QuantStudio 3 Real-Time PCR System (Thermo Fisher Scientific) using TB Green Premix Ex Taq II (Takara Bio). Thermal cycling consisted of: 95 °C for 30s, followed by 40 cycles of 95 °C for 5 s and 60 °C for 34s. Primer sequences are provided in Table 1. Relative gene expression was calculated using the 2^−ΔΔCt^ method, normalized to GAPDH.

Macrophage Polarization and Immunofluorescence Staining

Macrophage Polarization and Treatment

RAW264.7 macrophages (ATCC) were seeded into 24-well plates containing sterile glass coverslips at a density of 1×10^5 cells per well and allowed to adhere overnight. To induce M1 polarization, cells were stimulated with lipopolysaccharide (LPS, 100 ng/mL; Sigma-Aldrich) or H_2O_2 (200 μM) for 24 h in the presence or absence of PEG-HS/TiO_2 (100 μg/mL). Unstimulated cells receiving PBS served as the M0 control group.

Immunofluorescence Staining

Following treatment, cells were fixed, permeabilized, and blocked as described in Oxidative Stress-Induced Cellular Senescence Model. Cells were incubated overnight at 4 °C with primary antibodies diluted in 1% BSA: rat anti-mouse CD86 (M1 marker; 1:200; BioLegend, Cat# 105002) and goat anti-mouse CD206 (M2 marker; 1:200; R&D Systems). After washing, cells were incubated with Alexa Fluor 488-conjugated donkey anti-rat IgG (1:500; Thermo Fisher Scientific) and Alexa Fluor 594-conjugated donkey anti-goat IgG (1:500; Thermo Fisher Scientific) for 1 h at room temperature in the dark. Nuclei were counterstained with DAPI. Images were captured using a Leica TCS SP8 confocal laser scanning microscope. Fluorescence intensities were quantified using ImageJ software from ≥100 cells per condition across three independent biological replicates.

Metabolic Flux Analysis (Seahorse Assay)

Real-time measurements of extracellular acidification rate (ECAR) and oxygen consumption rate (OCR) were performed using a Seahorse XFe96 Extracellular Flux Analyzer (Agilent Technologies). RAW264.7 macrophages were seeded into Seahorse XF96 V3 PS microplates at 8×10^4 cells per well and allowed to adhere overnight. Cells were treated with PBS (control), H_2O_2 (200 μM), or H_2O_2 (200 μM) plus PEG-HS/TiO_2 (100 μg/mL) for 24 h. One hour prior to the assay, medium was replaced with Seahorse XF DMEM assay medium (pH 7.4) supplemented with glucose (10 mM), glutamine (2 mM), and sodium pyruvate (1 mM for ECAR; 2 mM for OCR). Cells were equilibrated at 37 °C in a non-CO_2 incubator for 45–60 min. For the Glycolysis Stress Test, compounds were sequentially injected: glucose (10 mM), oligomycin (1 μM), and 2-deoxy-D-glucose (50 mM). For the Mitochondrial Stress Test, injections were: oligomycin (1 μM), FCCP (1 μM), and rotenone/antimycin A (0.5 μM each). All reagents were obtained from Sigma-Aldrich. After the Seahorse assay, cells were lysed with RIPA buffer, and total protein concentration was determined using a BCA protein assay kit (Beyotime Biotechnology, Shanghai, China). Both ECAR and OCR values were normalized to total protein content (pmol/min/μg protein) to account for potential differences in cell density across wells. Data were analyzed using Wave Desktop software (Agilent Technologies).

Diabetic Murine Wound Healing Model

Animals

Male C57BL/6J mice (8–10 weeks old, 20–25 g) were obtained from the Laboratory Animal Center of Southern Medical University (Guangzhou, China). Mice were housed under specific pathogen-free (SPF) conditions in a temperature-controlled environment (22 ± 1 °C) with a 12 h light/dark cycle and provided ad libitum access to standard chow and autoclaved water. All animal procedures were approved by the Animal Research Ethics Committee of Nanfang Hospital, Southern Medical University (Approval No. NFYY-2025-0203) and conducted in strict accordance with the National Institutes of Health Guide for the Care and Use of Laboratory Animals and the ARRIVE guidelines.

Induction of Diabetes Mellitus

Following a 1-week acclimatization period, diabetes was induced by intraperitoneal injection of streptozotocin (STZ; Sigma-Aldrich) dissolved in freshly prepared citrate buffer (0.1 M, pH 4.5) at a dose of 50 mg/kg body weight for five consecutive days. Blood glucose levels were monitored from tail vein blood samples using an Accu-Chek Performa glucometer (Roche Diagnostics, Mannheim, Germany). Blood glucose levels were monitored from tail vein blood samples at 48 h, 72 h, and 7 days after the final STZ injection, and then weekly thereafter. Mice with non-fasting blood glucose levels exceeding 16.7 mM (300 mg/dL) for two consecutive measurements (at least 48 h apart) were considered diabetic and enrolled in wound healing studies. A minimum 2-week stabilization period (14 days) following STZ administration was observed prior to wound creation to ensure sustained hyperglycemia and metabolic stability.

Full-Thickness Excisional Wound Model

Diabetic mice were anesthetized via isoflurane inhalation using a veterinary anesthesia vaporizer. Induction was performed with 3% isoflurane delivered in 100% oxygen at a flow rate of 1 L/min. Maintenance anesthesia was achieved with 1.5–2% isoflurane in oxygen at 0.5–1 L/min. Anesthesia depth was confirmed by absence of pedal withdrawal reflex and regular breathing pattern. During the procedure, body temperature was maintained at 37 ± 0.5 °C using a heating pad. The dorsal skin was shaved using an electric clipper and depilated with hair removal cream. The surgical area was sterilized with 70% ethanol followed by povidone-iodine solution. Two full-thickness excisional wounds (6 mm diameter) were created on the dorsum of each mouse using a sterile disposable biopsy punch (Kai Medical, Solingen, Germany). The wounds were left uncovered throughout the experimental period.

Treatment Groups and Administration

Mice were randomly allocated into four experimental groups (n = 6 per group): (1) PBS vehicle control, (2) free TiO_2 nanoparticles (100 μg/mL), (3) free HS extract (equivalent HS concentration), and (4) PEG-HS/TiO_2 nanocomposite (100 μg/mL, based on HS content). All materials were freshly dispersed in sterile phosphate-buffered saline (PBS, pH 7.4) and sonicated for 10 minutes prior to each topical application to ensure uniform suspension. The concentration of HS in group (3) was matched to that loaded in group (4) as determined by the UV-Vis quantification method described in Physicochemical Characterization. Treatments (50 μL per wound) were applied topically to the wound bed using a micropipette immediately following wound creation and subsequently once daily for the first 7 days. To ensure prolonged contact between the formulation and the wound surface, a sterile, breathable, hypoallergenic transparent film dressing (Tegaderm™, 3M Health Care, St. Paul, MN, USA) was gently placed over the wound immediately after each application. The dressing was secured by adhering its edges to the surrounding intact skin, without applying excessive tension or compression to the wound bed. This dressing is permeable to water vapor and oxygen while providing a physical barrier that prevents mechanical removal of the formulation by bedding contact or animal movement. The dressing was replaced daily together with the next formulation application, during which the wound was gently cleaned with sterile saline if necessary. Wounds were photographed at predetermined time points (days 0, 3, 5, 7, 10, and 14 post-wounding) using a Canon EOS 80D digital camera (Canon Inc., Tokyo, Japan) equipped with a macro lens and fixed focal distance. A sterile ruler was included in each photograph for scale calibration.

Wound Closure Analysis

Wound area was quantified from digital photographs using ImageJ software. The wound margin was manually traced by two independent observers blinded to treatment allocation. Histological scoring was similarly performed by blinded observers. Wound area at each time point was expressed as a percentage of the initial wound area on day 0. Time to complete wound closure was defined as the number of days required for the wound bed to be completely covered by visible epithelial tissue.

Histological and Immunofluorescence Analysis of Wound Tissue

Tissue Harvesting and Processing

At designated time points (days 7, 14, and 28 post-wounding), mice were euthanized by carbon dioxide (CO_2) inhalation followed by cervical dislocation, in strict accordance with the American Veterinary Medical Association (AVMA) Guidelines for the Euthanasia of Animals. Briefly, mice were placed in a pre-filled induction chamber with CO_2 introduced at a controlled flow rate of 10–30% of the chamber volume per minute. Following loss of consciousness (confirmed by absence of righting reflex and lack of response to toe pinch), the CO_2 flow was maintained for at least 5 minutes after respiratory arrest. Death was confirmed by cessation of heartbeat and respiration, followed by cervical dislocation as a secondary physical method to ensure euthanasia. Wound tissue including the surrounding margin (approximately 1 cm) of unwounded skin was excised, bisected along the midline, and immediately fixed in 4% paraformaldehyde (Sigma-Aldrich) for 24 h at 4 °C. Fixed tissues were dehydrated through a graded ethanol series, cleared in xylene, and embedded in paraffin wax using a Leica TP1020 tissue processor (Leica Biosystems, Wetzlar, Germany). Paraffin-embedded blocks were sectioned at a thickness of 5 μm using a Leica RM2235 rotary microtome (Leica Biosystems).

Hematoxylin and Eosin (H&E) Staining. Deparaffinized and rehydrated tissue sections were stained with Mayer's hematoxylin solution (Sigma-Aldrich) for 5 min, rinsed in running tap water, differentiated in 1% acid alcohol, and blued in Scott's tap water substitute. Sections were then counterstained with eosin Y solution (Sigma-Aldrich) for 2 min, dehydrated, cleared, and mounted with DPX mounting medium (Sigma-Aldrich). Stained sections were imaged using an Olympus BX53 upright microscope (Olympus Corporation) equipped with a DP74 digital camera. Dermal thickness was quantified from H&E-stained sections using ImageJ software by measuring the vertical distance from the epidermal-dermal junction to the dermal-adipose layer interface at five equidistant points across each tissue section.

Masson's Trichrome Staining

Collagen deposition and organization were evaluated using a Masson's Trichrome Stain Kit (Sigma-Aldrich) according to the manufacturer's protocol. Stained sections were imaged as described above. Collagen volume fraction was quantified as the percentage of aniline blue-positive area relative to the total tissue area using ImageJ software.

Immunofluorescence Staining of Wound Sections

For immunofluorescence analysis, tissue sections were deparaffinized, rehydrated, and subjected to heat-induced antigen retrieval in citrate buffer (10 mM, pH 6.0) using a pressure cooker for 10 min. Sections were permeabilized with 0.3% Triton X-100 in PBS for 15 min and blocked with 5% BSA in PBS for 1 h at room temperature. Primary antibodies diluted in 1% BSA were applied overnight at 4 °C: rabbit anti-CD31 (endothelial cell marker; 1:100 dilution; Abcam), rat anti-CD86 (M1 macrophage marker; 1:100 dilution; BioLegend), rabbit anti-collagen I (1:200 dilution; Abcam), and rabbit anti-collagen III (1:200 dilution; Abcam). Following washing, sections were incubated with appropriate Alexa Fluor-conjugated secondary antibodies (1:500 dilution; Thermo Fisher Scientific) for 1 h at room temperature. Nuclei were counterstained with DAPI. Sections were mounted with ProLong Gold Antifade Mountant and imaged using the Leica TCS SP8 CLSM system. Fluorescence intensities and positive areas were quantified using ImageJ software from at least five randomly selected high-power fields per section.

Laser Speckle Contrast Imaging (LSCI)

Regional blood perfusion within the healed wound area was assessed non-invasively on day 28 post-wounding using a PeriCam PSI System laser speckle contrast imager (Perimed AB, Järfälla, Stockholm, Sweden). Mice were anesthetized with isoflurane and placed in a prone position on a heated imaging platform maintained at 37 °C. The wound region was imaged at a working distance of 10 cm with a 785 nm laser source. Perfusion images were acquired and analyzed using PIMSoft software version 2.4 (Perimed AB). A standardized region of interest (ROI) encompassing the healed wound area was defined for each animal, and mean perfusion units (PU) were calculated and expressed relative to an adjacent region of uninjured dorsal skin.

Systemic Inflammatory Marker Analysis

Whole blood was collected from the retro-orbital plexus of anesthetized mice at predetermined time intervals (days 0, 7, and 14 post-wounding) using serum separator tubes (BD Microtainer, Becton Dickinson). Blood samples were allowed to clot at room temperature for 30 min and then centrifuged at 3,000 rpm for 10 min at 4 °C to obtain serum. Serum concentrations of C-reactive protein (CRP) and procalcitonin (PCT) were quantified using commercially available enzyme-linked immunosorbent assay (ELISA) kits according to the manufacturers' protocols: Mouse CRP ELISA Kit (Abcam, Cambridge, UK) and Mouse PCT ELISA Kit (MyBioSource, San Diego, CA, USA). Absorbance was measured at 450 nm using the Thermo Fisher Multiskan FC microplate reader, and concentrations were interpolated from standard curves generated using recombinant protein standards.

In vivo Biosafety Evaluation

To evaluate potential systemic toxicity following topical application, major organs (heart, liver, spleen, lung, and kidney) were harvested from diabetic mice at 6 h, 24 h, and day 7 post-wounding. For Ti biodistribution analysis, approximately 100 mg of each organ was digested in concentrated nitric acid at 60 °C for 48 h, and titanium content was quantified by inductively coupled plasma mass spectrometry (ICP-MS; Agilent 7900, Agilent Technologies, Santa Clara, CA, USA). Additionally, peripheral blood was collected from the retro-orbital plexus at days 0, 7, 14, and 21 post-wounding. Complete blood counts (RBC, WBC, and PLT) were measured using an automated hematology analyzer (Mindray BC-5000, Shenzhen, China). Serum levels of IFN-γ and IL-1β were quantified by ELISA kits (R&D Systems, Minneapolis, MN, USA). Tissues were also fixed, processed, embedded in paraffin, sectioned, and stained with H&E for histopathological examination as described in Histological and Immunofluorescence Analysis of Wound Tissue. Histological sections were examined by a board-certified veterinary pathologist blinded to treatment allocation for any evidence of histopathological abnormalities, including inflammatory infiltrates, necrosis, fibrosis, or architectural distortion.

Statistical Analysis

All in vitro experiments were performed with a minimum of three independent biological replicates (n = 3 per group). This sample size was determined based on power analysis using the following parameters: expected effect size (Cohen's d = 2.5–3.0, estimated from preliminary experiments), desired power (0.85), and significance level ($\alpha = 0.05$, two-tailed). Under these assumptions, a minimum of 3–4 replicates per group is sufficient to detect a statistically significant difference with adequate power. For in vivo experiments, n = 6 per group was used to account for potential biological variability and to ensure robust statistical power (≥ 0.80) based on similar wound healing studies. Data are expressed as mean ± standard deviation (SD). Statistical analyses were conducted using GraphPad Prism software version 9.5 (GraphPad Software, San Diego, CA, USA). Normality of data distribution was assessed using the Shapiro–Wilk test. For comparisons between two groups, a two-tailed unpaired Student's *t*-test was employed. For comparisons among three or more groups, one-way analysis of variance (ANOVA) followed by Tukey's post hoc test for multiple comparisons was utilized.

Results and Discussion

Synthesis and Physicochemical Characterization of PEG-HS/TiO_2 Nanocomposites

The morphology and microstructural features of the as-prepared PEG-HS/TiO_2 nanocomposites were initially characterized by transmission electron microscopy (TEM). As presented in Figure 1B, the nanostructures exhibited a relatively uniform, popcorn-like spherical architecture. High-resolution TEM (HRTEM) analysis further elucidated the crystallographic characteristics, wherein distinct lattice fringes consistent with the anatase TiO_2 phase could be clearly discerned (Figure 1C). This observation was corroborated by energy-dispersive X-ray spectroscopy (EDS) elemental mapping (Figure 1D and F), which revealed a generally homogeneous spatial distribution of Ti, O, and elemental signatures associated with the organic honeysuckle (HS) component.

The bulk crystallographic properties were further validated by X-ray diffraction (XRD). The diffraction pattern obtained for PEG-HS/TiO_2 (Figure 1G) displayed characteristic peaks that align closely with the standard anatase phase (JCPDS No. 21–1272), suggesting that the incorporation of PEG and HS components does not appear to substantially perturb the intrinsic crystal structure of the TiO_2 core. Aberration-corrected high-angle annular dark-field scanning TEM (AC HAADF-STEM) imaging (Figure 1E) provided atomic-scale resolution, revealing intact lattice arrays with no obvious amorphous aggregation. This observation is consistent with the retention of structural integrity in the nanocomposite following surface modification. To ascertain the surface chemical environment, X-ray photoelectron spectroscopy (XPS) was performed. The survey spectrum (Figure 1H) indicated the presence of Ti 2p, O 1s, and C 1s signals, indicative of the expected elemental composition.

The textural properties of the nanocomposite were evaluated via nitrogen adsorption-desorption isotherm measurements (Figure 1I). The isotherm exhibited a Type IV profile with an H2-type hysteresis loop, a feature generally characteristic of mesoporous materials. The resultant specific surface area and pore volume are likely to provide potential adsorption sites for the HS moiety and, furthermore, may facilitate the diffusion of reactive oxygen species (ROS) toward active sites—a plausible prerequisite for efficient catalytic scavenging.

Optical characterization via ultraviolet-visible (UV-Vis) spectroscopy revealed that the absorbance profile of PEG-HS/TiO_2 retains the characteristic UV absorption peaks observed in the pure HS extract (Figure 1J), implying successful integration of the organic component. Furthermore, The hydrodynamic diameters of Cur-MSN and MSN were characterized by DLS. As shown in Figure 1K, Cur-MSN exhibited a monomodal size distribution with a mean diameter of 175.7 ± 1.2 nm and a PDI of 0.18, indicating narrow size distribution. MSN displayed a mean diameter of 191.5 ± 0.8 nm with a PDI of 0.22, along with a minor peak at ~270 nm (~20% intensity), suggesting the presence of a small fraction of larger aggregates. Both samples showed acceptable colloidal stability (PDI < 0.3). This change appears consistent with the formation of a hydrated polymer shell surrounding the inorganic core. To provide direct evidence of HS integration and its interaction with the PEGylated TiO_2 surface, FTIR spectroscopy was performed. As shown in Figure S1A (Supporting Information), the FTIR spectrum of PEG-HS/TiO_2 exhibited characteristic HS peaks (C=O at ~1710 cm^{-1} and aromatic C=C at ~1630 cm^{-1}), along with a notable shift of the PEG C–O–C peak from 1105 cm^{-1} to ~1112 cm^{-1} and subtle changes in Ti–O–Ti vibration bands compared to PEG-TiO_2, indicating hydrogen bonding interactions between HS and the nanocomposite; a physical mixture of HS and PEG-TiO_2 showed no such peak shifts, confirming genuine chemical binding rather than simple physical admixture. TGA analysis revealed that the HS loading content, calculated from the weight loss difference between PEG-HS/TiO_2 and PEG-TiO_2 in the HS decomposition temperature range (200–500 °C), was approximately 12.55 wt%, which is consistent with UV-Vis quantification (~11.9 wt%) (Figure S1B, Supporting Information). Zeta potential of bare TiO_2 was −18.3 ± 2.1 mV, shifting to −8.2 ± 1.5 mV after PEGylation (charge shielding) and further to −15.6 ± 2.3 mV after HS loading (phenolic hydroxyl groups), confirming successful surface modification (Figure S2). The mildly negative surface charge of PEG-HS/TiO_2 may favor colloidal stability and reduce nonspecific protein adsorption.

A critical parameter governing the therapeutic utility of this system is the release kinetics of the bioactive HS component. As depicted in Figure 1L, the release profile of HS from the nanocomposite exhibited a pronounced sustained-release pattern, extending up to 72 hours at both pH 5.5 and pH 7.4. Notably, the release rate was slightly faster at pH 5.5 compared to pH 7.4, particularly during the first 24 h, suggesting that the acidic microenvironment may

facilitate more rapid HS liberation. To gain insight into the release mechanism, the cumulative release data at pH 5.5 and pH 7.4 were fitted to zero-order, first-order, and Higuchi kinetic models. The release profiles at both pH conditions were best described by the first-order kinetic model (pH 7.4: $R^2 = 0.989$; pH 5.5: $R^2 = 0.994$), with release rate constants of 0.168 h^{-1} and 0.169 h^{-1}, respectively (Figure S3, Supporting Information). This pH-responsive behavior is potentially advantageous for diabetic wound healing, as it ensures higher HS availability during the early inflammatory phase when oxidative stress and bacterial burden are most pronounced, while maintaining sustained release at physiological pH thereafter. Such behavior is considered favorable for long-acting effects in topical wound applications, thereby potentially minimizing off-target effects in adjacent healthy tissue.

Collectively, these characterization data indicate that the PEG-HS/TiO_2 nanocomposite possesses a well-defined mesoporous anatase structure, robust organic-inorganic hybridization, and sustained-release characteristics. These attributes are expected to provide a sound material basis for the subsequent in vitro and in vivo biological evaluation.

Antioxidant Efficacy and Cytocompatibility of PEG-HS/TiO_2 Nanocomposites

Given the central role of excessive reactive oxygen species (ROS) in perpetuating chronic inflammation and delaying wound repair, the ability of a therapeutic nanomaterial to effectively neutralize these deleterious species represents a critical functional attribute. The antioxidant performance of PEG-HS/TiO_2 was therefore systematically evaluated using a combination of spectroscopic, enzymatic, and electron paramagnetic resonance (EPR) techniques. As illustrated schematically in Figure 2A, the nanocomposite is proposed to scavenge ROS via intrinsic superoxide dismutase (SOD)- and catalase (CAT)-mimetic activities, wherein the TiO_2 component likely serves as the primary catalytic center. To assess the structural stability of the nanocomposite under oxidative conditions, TEM imaging was performed after incubation in 5% H_2O_2 solution. As shown in Figure 2B, PEG-HS/TiO_2 exhibits significant degradation under physiologically relevant oxidative stress conditions due to catalytic reactions, which facilitates biodegradation in vivo. To directly probe the ROS-scavenging capacity, EPR spectroscopy was utilized in conjunction with spin-trapping agents. Under physiologically relevant pH conditions (pH 7.4), PEG-HS/TiO_2 treatment resulted in a marked attenuation of the characteristic O_2^- spin adduct signal compared to the untreated control (Figure 2C). Similarly, the EPR spectra corresponding to H_2O_2 revealed a substantial reduction in peak intensity upon exposure to the nanocomposite (Figure 2D). These findings provide compelling evidence that PEG-HS/TiO_2 is capable of efficiently quenching both superoxide anions and hydrogen peroxide, corroborating the proposed dual-enzyme mimetic mechanism. The H_2O_2 elimination capability was further quantified using a commercial peroxide assay kit. As shown in Figure 2E, a significant depletion of H_2O_2 was observed after a brief 10 min incubation period with PEG-HS/TiO_2 (***$p < 0.01$ at 75 μg/mL vs. 100 μg/mL). Complementary colorimetric analysis employing the WST-1 method (Figure 2F) confirmed a pronounced superoxide anion elimination rate (**$p < 0.01$ at 50 μg/mL vs. 75 μg/mL; ***$p < 0.001$ at 75 μg/mL vs. 100 μg/mL). Taken together, these quantitative assessments affirm that the nanocomposite exhibits robust ROS-neutralizing properties.

While potent antioxidant activity is desirable, the clinical translation of any nanomaterial hinges critically upon its biocompatibility and safety profile. To address this, the cytocompatibility of PEG-HS/TiO_2 was evaluated across three distinct mammalian cell lines—HaCaT keratinocytes, HUVEC endothelial cells, and L929 fibroblasts—representative of the major cell types involved in dermal wound healing. The MTT assay results (Figure 2G) indicated that exposure to varying concentrations of PEG-HS/TiO_2 did not elicit any appreciable cytotoxicity across the tested dose range. Cell viability remained consistently high, implying that the nanocomposite is well-tolerated by these therapeutically relevant cell populations. Hemocompatibility constitutes another essential facet of in vivo safety assessment. The hemolytic activity of 100 μg/mL PEG-HS/TiO_2 was examined across a gradient of concentrations (Figure 2H, $p > 0.05$). The hemolysis ratio remained well below the clinically accepted threshold (typically <5%) even at elevated concentrations, indicating negligible disruption to erythrocyte membrane integrity.

To further evaluate acute in vivo toxicity, a pilot histological examination was performed on major organs (heart, liver, spleen, lung, and kidney) harvested from diabetic mice following a 28-day regimen of topical nanocomposite administration. Representative hematoxylin and eosin (H&E)-stained sections (Figure 2I) revealed no discernible histopathological abnormalities, inflammatory infiltrates, or necrotic lesions in any of the examined tissues when compared to untreated controls. This preliminary finding lends support to the notion that topical application of PEG-

 https://doi.org/10.2147/IJN.S617254

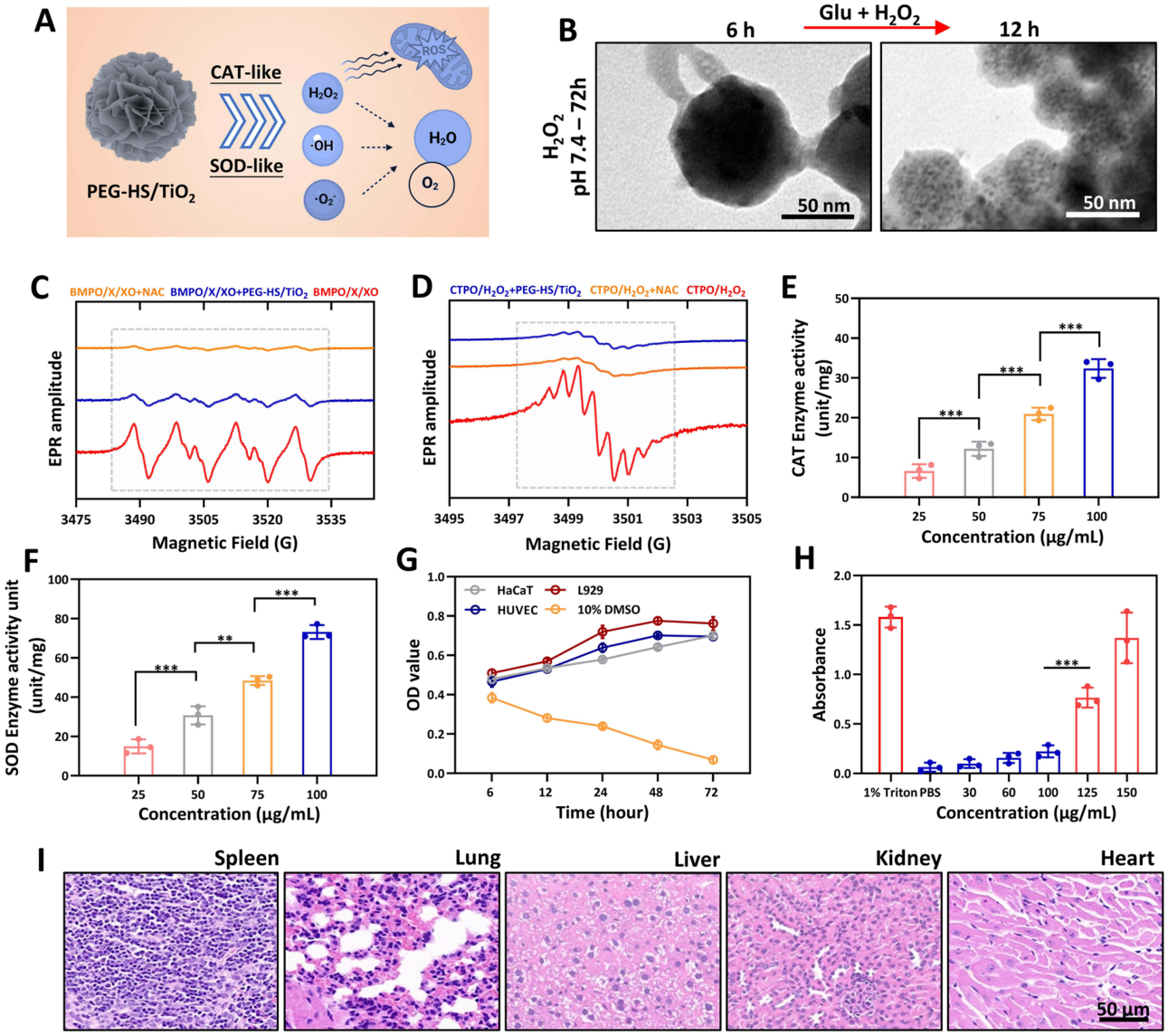

Figure 2 Antioxidant performance and cytocompatibility of PEG-HS/TiO_2. (**A**) Diagram depicting ROS neutralization by PEG-HS/TiO_2 through intrinsic SOD- and CAT-mimetic mechanisms. (**B**) TEM micrograph of PEG-HS/TiO_2 after immersion in 5% H_2O_2 aqueous medium. (**C**) EPR spectra illustrating O_2^- quenching by PEG-HS/TiO_2 at pH 7.4 (X: xanthine; XO: xanthine oxidase). (**D**) EPR assessment of H_2O_2 depletion efficacy of PEG-HS/TiO_2 under physiological pH. (**E**) Remaining H_2O_2 content determined after a 10 min reaction period using a commercial peroxide quantification kit. (**F**) Superoxide anion elimination rate analyzed via a colorimetric SOD assay (WST-1 protocol). (**G**) Dose-dependent viability of HaCaT, HUVEC, and L929 fibroblasts evaluated by MTT reduction following treatment with PEG-HS/TiO_2. (**H**) Concentration–response profile of hemolysis induced by PEG-HS/TiO_2 exposure. (**I**) Representative H&E-stained sections of principal organs excised from diabetic mice after 7 days of topical PEG-HS/TiO_2 administration. n = 3 independent biological replicates. Values represent mean ± SD; $^{**}p < 0.01$ and $^{***}p < 0.001$.

HS/TiO_2 is unlikely to induce systemic off-target toxicity under the tested conditions. To further evaluate the biosafety of PEG-HS/TiO_2, we assessed Ti biodistribution, hematological parameters, and systemic inflammatory markers. As shown in Table 2, trace amounts of Ti were detected in major organs at 6 h post-wounding, with peak accumulation observed at 24 h, followed by a marked decrease by day 7, indicating effective clearance of the nanocomposite. Notably, Ti levels in all organs remained below the detectable limit by day 28. Peripheral blood analysis (Figure S4A–C, Supporting Information) revealed no significant differences in RBC, WBC, or PLT counts among treatment groups at any time point (days 0, 7, 14, and 21), suggesting no hematological toxicity. Furthermore, serum levels of the pro-inflammatory cytokines IFN-γ and IL-1β (Figure S4D and E, Supporting Information) remained comparable between PEG-HS/TiO_2-treated and PBS control groups throughout the 21-day observation period, indicating that topical application of the

Table 2 ICP-MS Analysis of Ti Biodistribution

Time Point	Wound	Liver	Spleen	Kidney	Lung	Heart
6 h	100%	BDL	BDL	BDL	BDL	BDL
24 h	48.4 ± 3.2%	BDL	BDL	BDL	BDL	BDL
7 d	4.3 ± 1.7%	BDL	BDL	BDL	BDL	BDL

Note: (< 0.1 ng/g tissue); values are expressed as percentage of total Ru applied.
Abbreviation: BDL, below detection limit.

nanocomposite does not induce a sustained systemic inflammatory response. Collectively, these data, together with the H&E staining results (Figure 2I), confirm the favorable in vivo biosafety profile of PEG-HS/TiO_2.

In summary, the data presented in this section establish that PEG-HS/TiO_2 functions as a potent dual-enzyme mimetic capable of effectively scavenging both superoxide and hydrogen peroxide. Moreover, the nanocomposite demonstrates excellent in vitro cytocompatibility, favorable hemocompatibility, and an apparently benign acute in vivo safety profile. These collective attributes strongly support its potential utility as a safe and efficacious local antioxidant therapeutic for the management of oxidative stress-implicated conditions such as chronic diabetic wounds.

PEG-HS/TiO_2 Attenuates Cellular Senescence and Promotes Proliferation via Modulation of Intracellular and Mitochondrial ROS

Endothelial cell dysfunction, frequently driven by persistent oxidative stress, is a hallmark of impaired wound healing in diabetic conditions.[28] Excessive accumulation of intracellular and mitochondrial reactive oxygen species (ROS) can precipitate premature cellular senescence, thereby compromising angiogenesis and tissue regeneration. Having established the robust ROS-scavenging capacity of PEG-HS/TiO_2 in acellular systems, we next sought to investigate whether this antioxidant functionality could be translated into tangible cytoprotective and pro-regenerative effects within a relevant cellular context.

Efficient cellular internalization is a prerequisite for nanomaterials intended to modulate intracellular redox homeostasis. Confocal laser scanning microscopy (CLSM) was therefore employed to visualize the uptake of rhodamine-labeled PEG-HS/TiO_2 by endothelial cells in 3, 12 an 24h. As shown in Figure 3A, the fluorescence signal gradually accumulated over time within the cytoplasmic compartment: significant uptake was observed at 3 hours, further intensified at 12 hours, and reached its peak at 24 hours. Fluorescence intensity analysis of cellular uptake efficiency (Figure 3B) confirmed these findings, demonstrating a continuous increase in the proportion of PEG-HS/TiO_2-positive cells throughout the incubation period: 40.98 at 3 hours, rising to 145.90 at 12 hours, and reaching 210.04 at 24 hours. This efficient internalization likely facilitates direct access of the nanocomposite to intracellular ROS pools, including those generated within the mitochondrial compartment. The CCK-8 assay results (Figure 3C) demonstrated that PEG-HS/TiO_2 significantly enhanced cell viability.

We next examined the capacity of PEG-HS/TiO_2 to mitigate oxidative stress-induced cellular senescence. Endothelial cells were challenged with hydrogen peroxide to establish a senescent phenotype, followed by treatment with the nanocomposite. Representative CLSM micrographs (Figure 3D) depicted senescence-associated β-galactosidase (SA-β-Gal) staining and p21 immunofluorescence under the different experimental conditions. Qualitative inspection revealed a notable diminution in both SA-β-Gal activity and p21 nuclear accumulation in cultures receiving PEG-HS/TiO_2 compared to the untreated H_2O_2-challenged group. Statistical quantification of these images (Figures 3E and F) confirmed a significant reduction in the percentage of senescent cells and a concomitant attenuation of p21 fluorescence intensity. These data strongly imply that PEG-HS/TiO_2 treatment effectively counteracts the progression of oxidative stress-induced premature senescence in endothelial cells.

Given the intimate association between cellular senescence and impaired angiogenic potential, we further probed the transcriptional expression of vascular endothelial growth factor (VEGF), a master regulator of angiogenesis. PCR analysis (Figure 3G) revealed that VEGF transcript levels were markedly elevated in cells treated with PEG-HS/TiO_2 relative to those exposed to H_2O_2 alone. This upregulation of a pro-angiogenic factor is consistent with the notion that

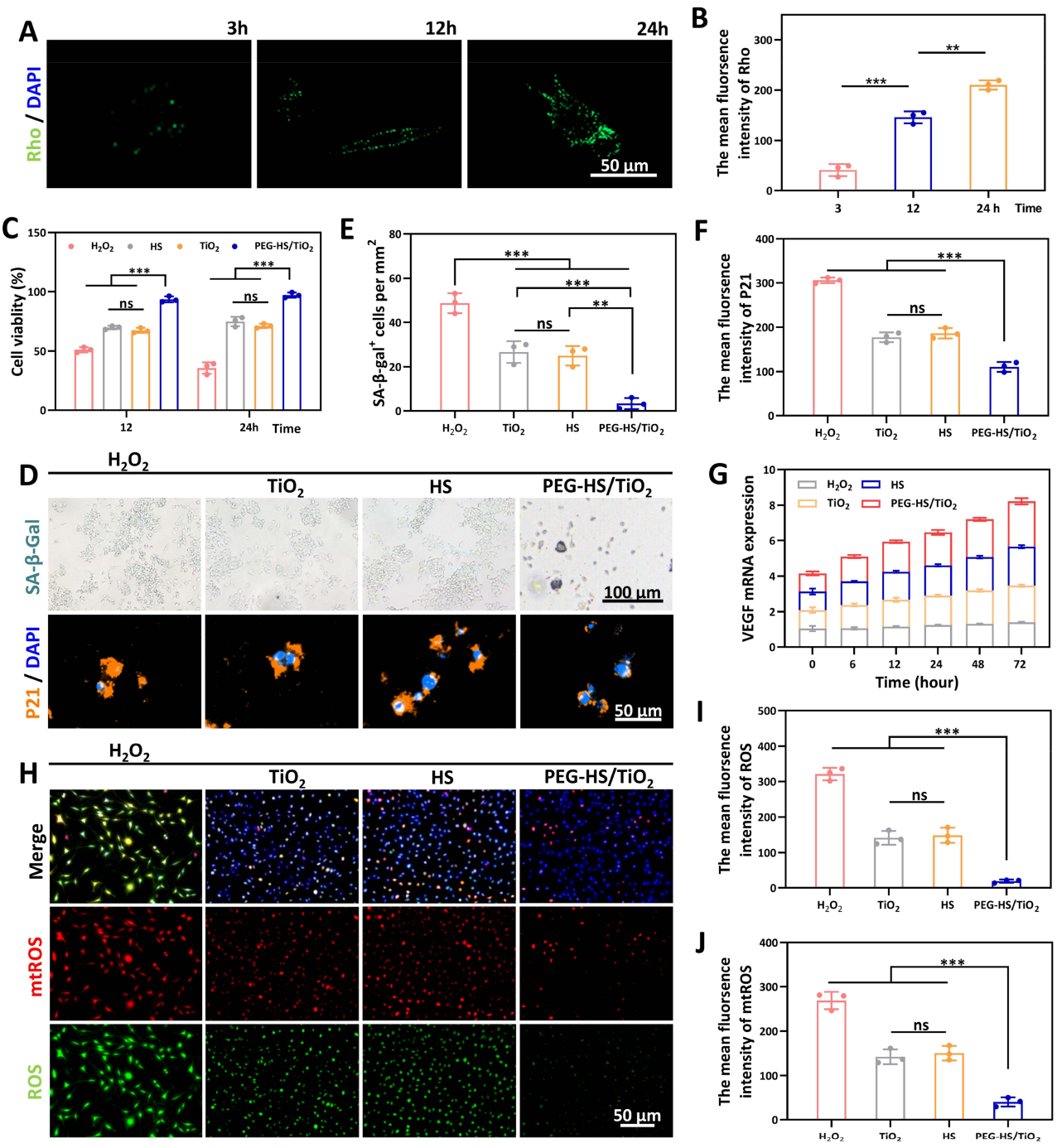

Figure 3 PEG-HS/TiO_2 alleviates cellular senescence and facilitates proliferation via attenuation of intracellular and mitochondrial ROS. (**A**) Quantitative assessment of rhodamine-labeled PEG-HS/TiO_2 internalization in endothelial cells visualized by confocal laser scanning microscopy (CLSM). (**B**) Corresponding analysis of cellular uptake efficiency. (**C**) Viability of endothelial cells following exposure to various material formulations, as determined by CCK-8 assay. (**D**) Representative CLSM micrographs depicting senescence-associated β-galactosidase (SA-β-Gal) staining and p21 expression in endothelial cells under different treatment regimens. (**E**–**F**) Statistical quantification of (**E**) senescent cell population and (**F**) p21 senescence marker levels presented in panel (D). (**G**) Transcriptional expression of VEGF evaluated by PCR. (**H**) Representative fluorescence images illustrating intracellular reactive oxygen species (ROS) and mitochondrial superoxide (mtROS) levels in endothelial cells. (**I-J**) Quantified fluorescence intensities corresponding to (**I**) total ROS and (**J**) mtROS burdens. n = 3 biologically independent samples. Data are expressed as mean ± SD; ns = no significant, $^{**}p < 0.01$ and $^{***}p < 0.001$.

alleviation of senescence-associated secretory phenotype (SASP) and restoration of cellular homeostasis can re-activate regenerative gene expression programs.

To establish a mechanistic link between the observed phenotypic outcomes and the intrinsic antioxidant properties of the nanocomposite, we directly visualized and quantified intracellular and mitochondrial ROS levels using fluorescent

https://doi.org/10.2147/IJN.S617254

probes. Representative fluorescence images (Figure 3H) demonstrated a substantial abrogation of both total intracellular ROS (detected by DCFH-DA) and mitochondrial superoxide (detected by MitoSOX Red) signals in PEG-HS/TiO_2-treated cells compared to the H_2O_2-challenged controls. Quantitative analysis of fluorescence intensities (Figure 3I and J) validated these observations, showing a pronounced decrease in both ROS burdens. The concurrent reduction of cytosolic and mitochondrial ROS suggests that the nanocomposite is capable of accessing and neutralizing oxidants within multiple subcellular compartments, with the attenuation of mitochondrial superoxide being particularly relevant given the established role of mitochondrial dysfunction in driving cellular senescence.[29,30]

Collectively, the findings presented in this section demonstrate that PEG-HS/TiO_2 is efficiently internalized by endothelial cells and exerts a multifaceted cytoprotective effect. By effectively quenching intracellular and mitochondrial ROS, the nanocomposite mitigates the acquisition of a senescent phenotype, as evidenced by reduced SA-β-Gal activity and p21 expression, and concomitantly promotes a pro-regenerative state characterized by enhanced VEGF transcription. These cellular-level observations provide a mechanistic rationale for the potential therapeutic benefits of PEG-HS/TiO_2 in promoting angiogenesis and tissue repair within the hostile oxidative microenvironment of chronic diabetic wounds.

PEG-HS/TiO_2 Promotes Macrophage M2 Polarization via Glycolytic Metabolic Reprogramming and Suppresses Pro-Inflammatory Cytokine Expression

Macrophages serve as central orchestrators of the wound healing cascade, with their phenotypic plasticity dictating the transition from the initial inflammatory phase to the subsequent proliferative and remodeling stages. Persistent hyperglycemia and oxidative stress in the diabetic microenvironment frequently drive macrophages toward a sustained pro-inflammatory (M1) phenotype, thereby perpetuating chronic inflammation and impairing tissue repair.[31] Given the robust ROS-scavenging properties of PEG-HS/TiO_2 established in preceding sections, we hypothesized that the nanocomposite might favorably modulate macrophage polarization and function through redox-dependent metabolic reprogramming.

To evaluate the influence of PEG-HS/TiO_2 on macrophage phenotype, we first examined the expression of canonical M1 and M2 surface markers by confocal laser scanning microscopy (CLSM). As illustrated in Figure 4A, macrophages exposed to lipopolysaccharide (LPS) exhibited pronounced CD86 immunoreactivity, indicative of M1 polarization, whereas CD206 expression remained relatively subdued. In marked contrast, co-treatment with PEG-HS/TiO_2 resulted in a notable diminution of CD86 signal accompanied by a concomitant enhancement of CD206 immunostaining. Quantitative analysis of fluorescence intensities (Figures 4F and G) corroborated these qualitative observations, revealing a significant shift in the M1/M2 marker ratio toward a predominantly M2-like phenotype. These findings suggest that PEG-HS/TiO_2 is capable of redirecting macrophage polarization away from a pro-inflammatory M1 state and toward a anti-inflammatory M2 state, even in the presence of potent M1-polarizing stimuli.

The functional consequences of this phenotypic shift were subsequently assessed by quantifying the transcriptional expression of key inflammatory and anti-inflammatory cytokines. As anticipated, LPS stimulation markedly upregulated transcript levels of the prototypical pro-inflammatory cytokines IL-1β, IL-6, and IFN-γ (Figures 4B–D). Conversely, co-incubation with PEG-HS/TiO_2 substantially attenuated this LPS-driven induction, with transcript abundance returning to levels approaching those of unstimulated controls. Notably, expression of the anti-inflammatory cytokine IL-10 (Figure 4E) was significantly elevated in PEG-HS/TiO_2-treated macrophages compared to both PBS and LPS-alone groups. This reciprocal regulation of pro- and anti-inflammatory mediators is consistent with a functional transition toward a resolving, tissue-reparative macrophage phenotype.

Emerging evidence has established a close mechanistic coupling between cellular metabolism and immune effector function, wherein M1 polarization is typically associated with enhanced glycolytic flux, while M2 polarization tends to favor oxidative phosphorylation. To investigate whether PEG-HS/TiO_2 exerts its immunomodulatory effects through metabolic reprogramming, we performed real-time measurements of extracellular acidification rate (ECAR) and oxygen consumption rate (OCR) in macrophages. As depicted in Figures 4G–I, H_2O_2 stimulation induced a robust increase in basal ECAR, reflecting the characteristic glycolytic switch accompanying M1 activation. Strikingly, co-treatment with PEG-HS/TiO_2 largely normalized this elevated glycolytic rate, reducing ECAR to levels comparable to those observed in PBS-treated controls. Complementary OCR analysis (Figures 4H–J) revealed that PEG-HS/TiO_2 co-treatment partially

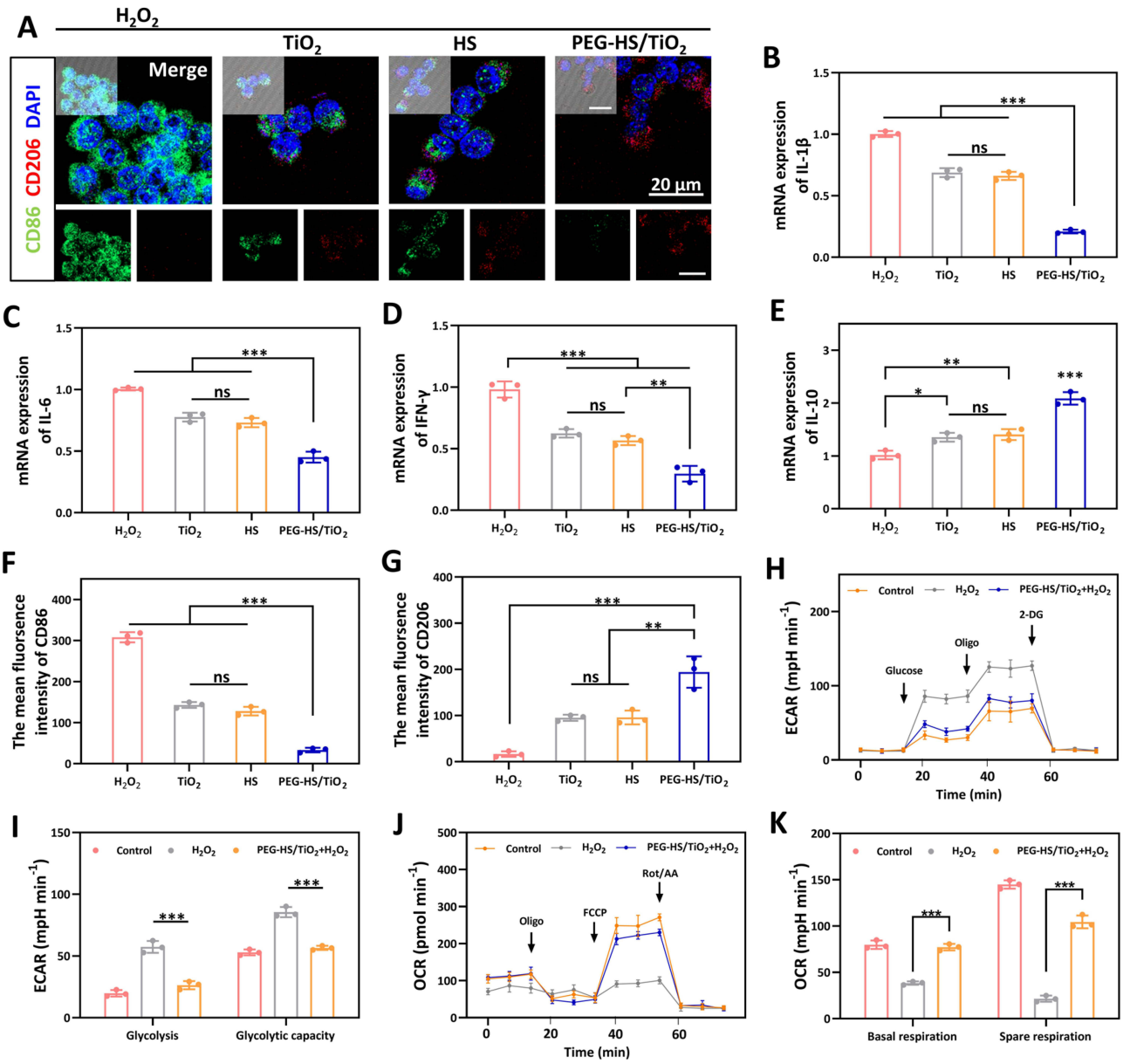

Figure 4 PEG-HS/TiO_2 directs macrophage polarization through glycolytic metabolic reprogramming and attenuates inflammatory cytokine expression. (**A**) Representative CLSM images illustrating CD206 (M2 marker) and CD86 (M1 marker) immunostaining in macrophages under different treatment conditions. Scale bar = 20 μm. (**B**–**E**) qPCR analysis of inflammatory cytokine transcript levels in macrophages subjected to different coculture conditions: (**B**) IL-1β, (**C**) IL-6, (**D**) IFN-γ, and (**E**) IL-10. (**F**–**G**) Quantitative assessments of fluorescence intensities corresponding to CD86 (**F**) and CD206 (**G**) from panel (A). (**H**–**I**) Extracellular acidification rate (ECAR) profiles of macrophages exposed to PBS, LPS, or LPS + PEG-HS/TiO_2, measured via glycolytic stress test (**H**) and mitochondrial stress test (**I**). (**J**–**K**) Oxygen consumption rate (OCR) traces for macrophages under the same treatment regimens, measured via glycolytic stress test (**J**) and mitochondrial stress test (**K**). Data are presented as mean ± SD; ns, not significant; *p < 0.05, **p < 0.01, ***p < 0.001. n = 3 independent biological replicates.

Abbreviations: 2-DG, 2-deoxyglucose; FCCP, carbonyl cyanide-p-trifluoromethoxyphenylhydrazone; Oligo, oligomycin; Rot/AA, rotenone + antimycin A.

preserved mitochondrial respiratory function, which was otherwise modestly impaired by H_2O_2 exposure. Of particular relevance to the antioxidant functionality of the nanocomposite, similar metabolic alterations were observed when macrophages were challenged directly with H_2O_2. As shown in Figures 4K, H_2O_2 exposure elicited a notable elevation in ECAR, suggesting that oxidative stress alone is sufficient to induce glycolytic upregulation in macrophages. Importantly, co-incubation with PEG-HS/TiO_2 effectively tempered this H_2O_2-driven metabolic shift, returning glycolytic activity toward baseline levels. Quantitative derivation of glycolytic capacity from these ECAR traces confirmed that PEG-HS/TiO_2 treatment significantly restrained the maximal glycolytic potential otherwise unleashed by H_2O_2

https://doi.org/10.2147/IJN.S617254

challenge. Correspondingly, spare respiratory capacity—a measure of mitochondrial fitness and metabolic flexibility—was substantially preserved in the presence of PEG-HS/TiO_2 compared to H_2O_2 treatment alone.

The parallel metabolic responses observed in H_2O_2-stimulated macrophages collectively imply that PEG-HS/TiO_2 may act through a common redox-sensitive mechanism to counterbalance the pro-glycolytic metabolic skew induced by diverse inflammatory and oxidative insults. This metabolic normalization appears conducive to M2 polarization and resolution of inflammation. The mechanistic link between ROS scavenging and metabolic reprogramming likely resides in the ability of PEG-HS/TiO_2 to diminish intracellular oxidant burdens—including those directly generated by exogenous H_2O_2—that would otherwise stabilize hypoxia-inducible factor 1-alpha (HIF-1α) and drive the transcriptional activation of glycolytic enzymes. As shown in Figure S5A–B (Supporting Information), immunofluorescence staining revealed that H_2O_2 treatment markedly increased the nuclear accumulation of HIF-1α compared with the PBS control group, indicating stabilization and activation of HIF-1α. In contrast, co-treatment with PEG-HS/TiO_2 significantly reduced the nuclear translocation of HIF-1α, with fluorescence intensity comparable to that of the control group. Consistent with the downregulation of HIF-1α, qPCR analysis (Figure S5C, Supporting Information) demonstrated that H_2O_2 treatment significantly elevated the mRNA levels of LDHA and PDK1 compared with the PBS control group, whereas co-treatment with PEG-HS/TiO_2 reversed these increases.

By attenuating this redox-sensitive signaling axis, the nanocomposite appears to facilitate a metabolic shift away from aerobic glycolysis and toward a more balanced bioenergetic state, which in turn supports the acquisition of an anti-inflammatory, pro-resolving macrophage phenotype. In summary, the data presented in this section demonstrate that PEG-HS/TiO_2 effectively reprograms macrophage polarization from a pro-inflammatory M1 toward a pro-regenerative M2 phenotype. This immunomodulatory effect is accompanied by a pronounced suppression of pro-inflammatory cytokine expression and correlates with a normalization of glycolytic metabolism coupled with preservation of mitochondrial respiratory capacity. Notably, these protective metabolic effects are recapitulated under direct H_2O_2 challenge, underscoring the functional importance of the nanocomposite's intrinsic ROS-scavenging activity in mediating immunometabolic reprogramming. These findings provide a compelling rationale for the application of PEG-HS/TiO_2 as an immunometabolic modulator capable of fostering a favorable wound healing microenvironment through the resolution of maladaptive inflammation.

Compared with previously reported nanozyme-based wound dressings that primarily focus on ROS scavenging or antimicrobial activity, our PEG-HS/TiO_2 nanocomposite offers several distinct advantages. First, the integration of HS phytochemicals provides sustained anti-inflammatory and antioxidant effects beyond the catalytic activity of TiO_2 alone, as evidenced by the 72 h release profile and FTIR-confirmed chemical binding. Second, while several studies have reported M2 polarization induced by nanomaterials, the underlying immunometabolic mechanism—specifically, the link between ROS scavenging, HIF-1α stabilization, and glycolytic reprogramming—has remained largely speculative. Our study provides direct experimental evidence (immunofluorescence and qPCR for HIF-1α, LDHA, and PDK1) supporting this mechanistic axis. Third, unlike systemically administered nanomedicines that may cause off-target toxicity, our topical application strategy, combined with comprehensive biosafety data (ICP-MS, CBC, and cytokine profiles), supports a favorable safety profile for clinical translation.

Mechanistic considerations and limitations. While our data demonstrate that PEG-HS/TiO_2 reduces HIF-1α nuclear translocation and downregulates LDHA/PDK1 expression, establishing a direct causal link between these observations requires additional experimental approaches. Specifically, future studies using HIF-1α knockdown (siRNA) or pharmacological inhibitors (eg., PX-478) are needed to confirm whether HIF-1α inhibition is necessary and sufficient for the observed metabolic reprogramming and M2 polarization. Additionally, whether other redox-sensitive transcription factors (eg., NF-κB, Nrf2) contribute to the immunomodulatory effects of PEG-HS/TiO_2 remains to be explored. Therefore, the proposed HIF-1α-centered mechanism should be interpreted as a plausible model supported by correlative evidence, rather than a definitive causal pathway.

PEG-HS/TiO_2 Accelerates Diabetic Wound Closure and Promotes Tissue Regeneration In Vivo

The favorable antioxidant capacity, cytocompatibility, and immunomodulatory properties of PEG-HS/TiO_2 established in the preceding in vitro investigations prompted us to evaluate its therapeutic potential in a clinically relevant animal model. Given that chronic diabetic wounds are characterized by persistent oxidative stress, prolonged inflammation, and impaired neovascularization, we sought to determine whether topical application of PEG-HS/TiO_2 could effectively ameliorate these pathological features and accelerate wound closure in vivo. The experimental protocol and treatment regimen are illustrated schematically in Figure 5A. Full-thickness excisional wounds were created on the dorsum of diabetic mice, followed by topical administration of either PBS vehicle control, free TiO_2, HS extract, or PEG-HS/TiO_2 nanocomposite at designated time intervals. Wound area quantification and histological scoring were performed by two

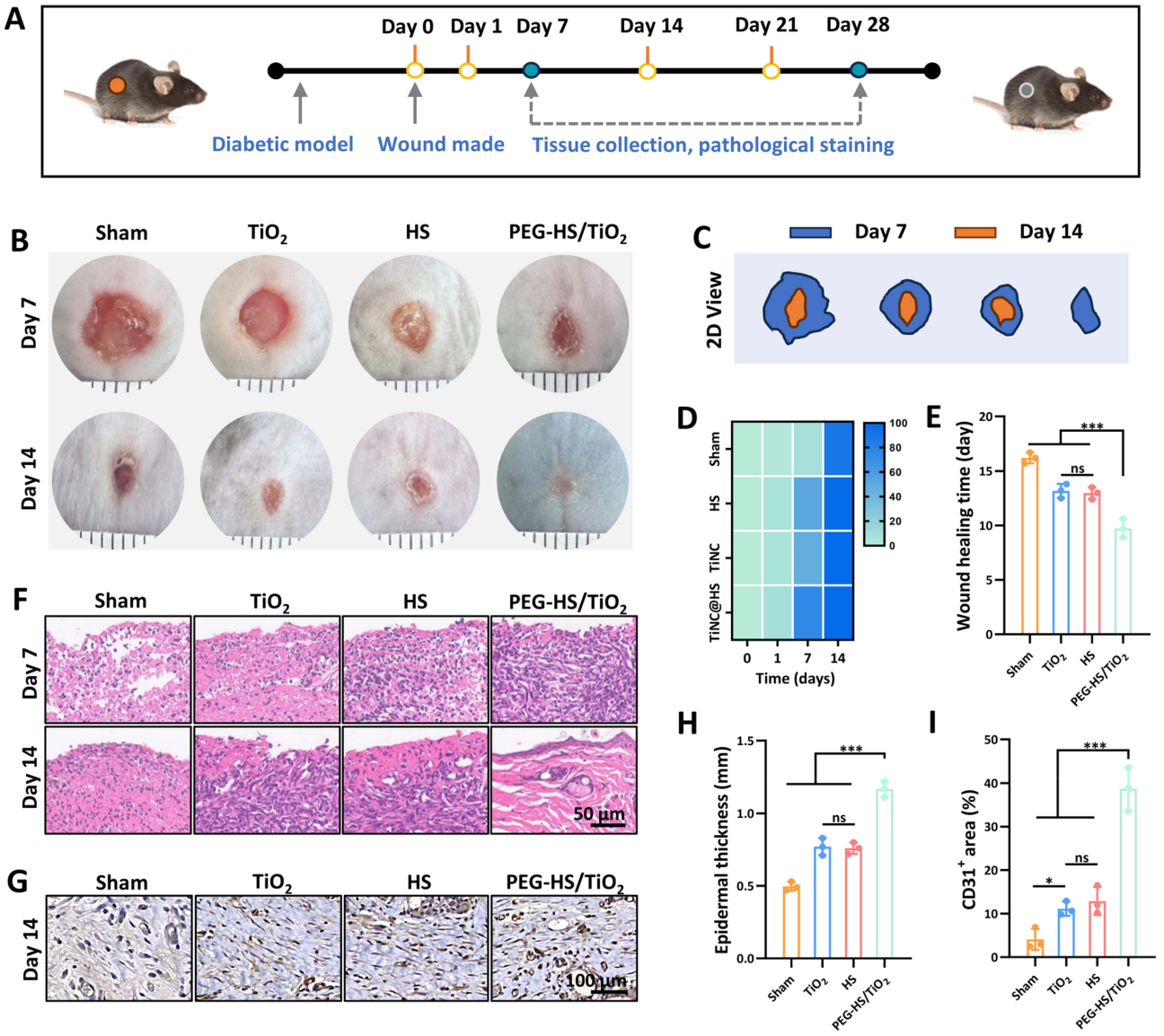

Figure 5 Evaluation of PEG-HS/TiO_2 efficacy on diabetic wound closure in vivo. (**A**) Schematic timeline of the animal experimental protocol and treatment regimen; The gray circle indicates healing, while the Orange circle indicates a wound site. (**B**) Representative photographic documentation of excisional wounds at designated time points post-treatment. (**C**) Quantitative analysis of wound area employing two-dimensional reconstruction techniques. (**D**) Temporal progression of wound area reduction across different therapeutic groups. (**E**) Wound closure duration for each experimental cohort. (**F**) Representative H&E-stained histological sections of wound tissue harvested on day 7 and 14. (**G**) Representative images of immunohistochemistry illustrating CD31 expression in wound beds on day 14. (**H**) Quantitative assessment of dermal thickness. (**I**) Morphometric quantification of vascularized regions (CD31-positive area). Data are presented as mean ± SD; ns, not significant; *$p < 0.05$ and ***$p < 0.001$. n = 3 independent biological replicates.

https://doi.org/10.2147/IJN.S617254

independent observers blinded to the treatment allocation, as detailed in Diabetic Murine Wound Healing Model (Figure S6, Supporting Information).

Serial documentation of the wound beds was performed at days 0, 3, 5, 7, 10, and 14 post-wounding to monitor the gross healing trajectory. Representative images at days 0, 7, and 14 are shown in Figure 5B; the full quantitative data for all time points are presented in Figure 5D and E. As shown in Figure 5B, wounds treated with PEG-HS/TiO_2 exhibited a visibly accelerated rate of contraction and re-epithelialization compared to both PBS and free HS groups, with this divergence becoming increasingly apparent at later time points. Quantitative analysis of wound area using two-dimensional reconstruction techniques (Figure 5C) corroborated these visual impressions. The temporal progression of wound area reduction (Figure 5D) revealed that PEG-HS/TiO_2-treated animals demonstrated significantly faster wound closure kinetics relative to control cohorts, with the disparity reaching statistical significance as early as day 5 post-wounding and becoming more pronounced by day 10. Notably, the time required to achieve complete wound closure was substantially abbreviated in the PEG-HS/TiO_2 group (Figure 5E–Figure 5H), with a mean closure time approximately 30% shorter than that observed in PBS-treated controls. These findings strongly imply that the nanocomposite is capable of expediting the overall wound healing process in the diabetic milieu. To gain mechanistic insight into the enhanced healing response, histological examination of wound tissue sections was performed at defined post-injury intervals. Hematoxylin and eosin (H&E) staining of tissue harvested on day 7 (Figure 5F) revealed striking differences in the extent of granulation tissue formation and re-epithelialization across treatment groups. Wounds receiving PEG-HS/TiO_2 displayed a more organized epithelial layer and enhanced dermal remodeling compared to controls on day 14, which exhibited relatively delayed tissue restoration and persistent inflammatory infiltrates. Quantitative assessment of dermal thickness (Figure 5H; Figure S7, Supporting Information) confirmed a significant increase in the PEG-HS/TiO_2-treated group, consistent with improved structural regeneration of the dermal compartment.

Given the critical role of angiogenesis in supplying oxygen and nutrients to the regenerating tissue, we next evaluated neovascularization within the wound bed by immunofluorescence staining for CD31, a well-established endothelial cell marker. Representative micrographs of day 14 wound sections (Figure 5G) depicted a notably higher density of CD31-positive area in animals treated with PEG-HS/TiO_2 compared to control groups. Morphometric quantification of vascularized regions (Figure 5I) validated this observation, demonstrating a robust and statistically significant increase in CD31-positive area in the nanocomposite-treated cohort. This pronounced pro-angiogenic effect is likely attributable to a combination of factors, including the alleviation of oxidative stress-mediated endothelial dysfunction, the restoration of VEGF expression as observed in vitro (Figure 3G), and the favorable immunomodulatory milieu established by M2-polarized macrophages.

The collective in vivo data provide compelling evidence that topical application of PEG-HS/TiO_2 effectively accelerates diabetic wound closure through a multifaceted mechanism involving enhanced re-epithelialization, improved dermal remodeling, and robust stimulation of neovascularization. The therapeutic benefits observed with PEG-HS/TiO_2 treatment surpassed those achieved with free HS extract alone, underscoring the advantages conferred by the nanocomposite architecture—namely, the sustained release kinetics and the synergistic interplay between the ROS-scavenging TiO_2 core and the bioactive HS component. These results align favorably with the in vitro characterization data, suggesting that the nanocomposite's capacity to neutralize oxidative stress and modulate local immune responses translates into tangible improvements in wound healing outcomes under diabetic conditions.

PEG-HS/TiO_2 Attenuates Systemic Inflammatory Markers and Improves Wound Prognosis via Local Immunomodulation

At day 28 post-wounding, we evaluated long-term tissue remodeling and wound maturation using Masson's trichrome staining and COL I/COL III immunofluorescence, as described in Histological and Immunofluorescence Analysis of Wound Tissue. While accelerated wound closure and enhanced tissue regeneration represent critical therapeutic endpoints, the long-term functional and structural quality of the healed tissue—often termed wound prognosis—is equally important in the clinical management of chronic diabetic ulcers. Inadequate resolution of inflammation during the healing cascade frequently results in aberrant scar formation, compromised tensile strength, and a heightened propensity for re-

ulceration. Having demonstrated that PEG-HS/TiO_2 accelerates wound closure and promotes neovascularization (PEG-HS/TiO_2 Accelerates Diabetic Wound Closure and Promotes Tissue Regeneration In Vivo), we next sought to evaluate whether these macroscopic improvements were accompanied by favorable alterations in systemic inflammatory status, local immune milieu, and ultimate tissue remodeling outcomes.

Systemic inflammatory burden was assessed by quantifying serum concentrations of C-reactive protein (CRP) and procalcitonin (PCT), two well-established circulating biomarkers of inflammation and infection. As depicted in Figure 6A and B, diabetic mice bearing excisional wounds exhibited modestly elevated serum CRP and PCT levels

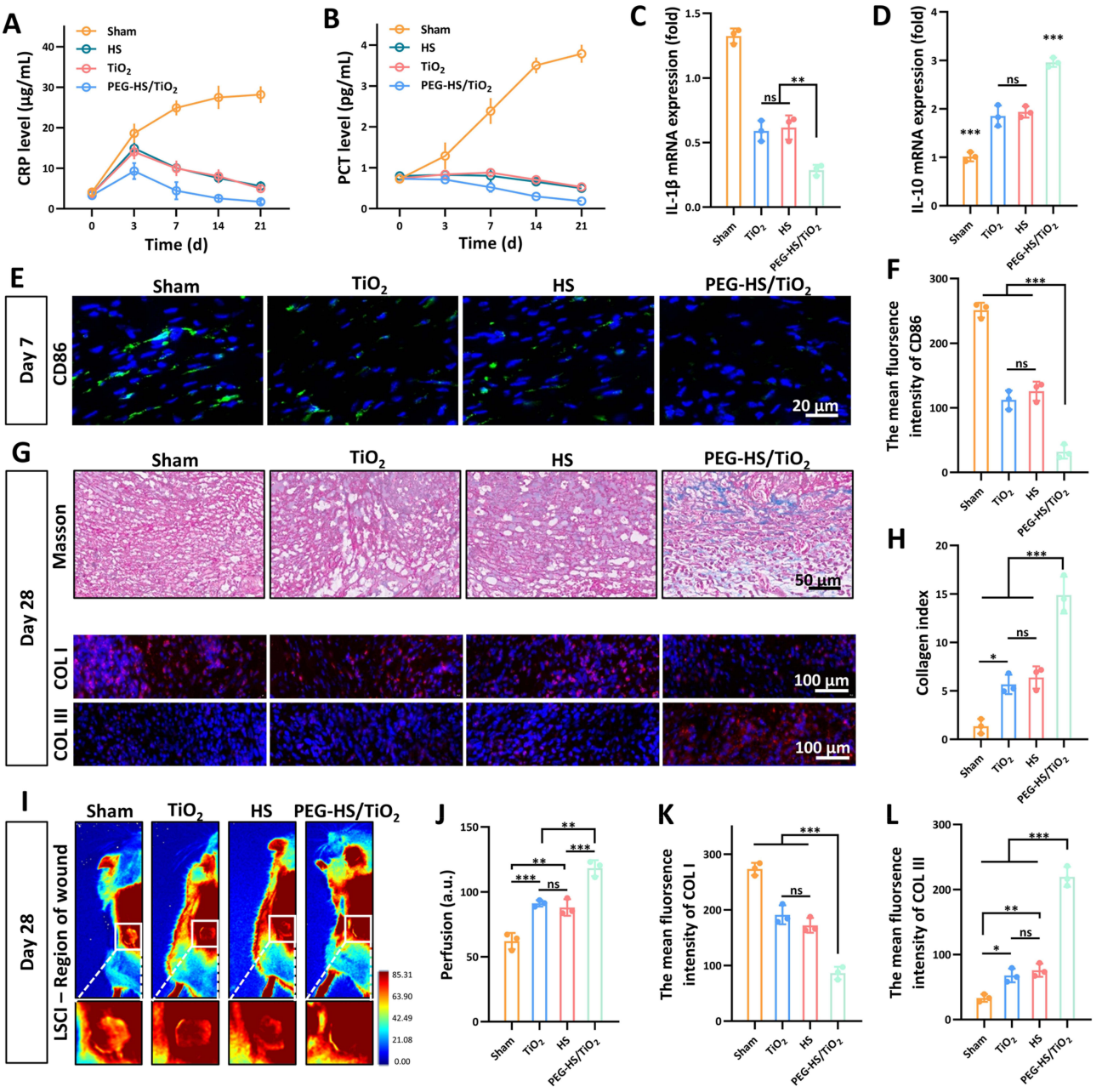

Figure 6 PEG-HS/TiO_2 attenuates systemic inflammatory markers and improves wound prognosis by modulating local macrophage polarization and cytokine expression. (**A**) Serum C-reactive protein (CRP) and (**B**) serum procalcitonin (PCT) concentrations in mice from different treatment cohorts at predetermined time intervals. (**C–D**) Quantitative PCR analysis of inflammatory cytokine transcript abundance in wound tissue homogenates: (**C**) anti-inflammatory cytokine IL-10, (**D**) pro-inflammatory cytokine IL-1β. (**E**) Representative CLSM immunofluorescence images depicting CD86 (M1 macrophage marker) expression in wound sections on day 7, with (**F**) corresponding quantitative evaluation. (**G**) Representative Masson's trichrome staining and COL I/COL III immunohistochemical visualization of wound tissue on day 28 across treatment groups. (**H**) Quantification of collagen volume fraction based on histological staining presented in panel (G). (**I**) Laser speckle contrast imaging (LSCI) of the wound region on day 28 for each experimental condition, and (**J**) subsequent analysis of regional blood perfusion dynamics. (**K–L**) Fluorescence intensity quantification corresponding to COL I and COL III immunostaining. Data are presented as mean ± SD; ns, not significant; *$p < 0.05$, **$p < 0.01$, ***$p < 0.001$.

https://doi.org/10.2147/IJN.S617254

compared to unwounded controls, consistent with a low-grade systemic inflammatory response secondary to local tissue injury. Notably, topical treatment with PEG-HS/TiO_2 resulted in a progressive and significant reduction in both CRP and PCT concentrations over the predetermined time course, with levels approaching those observed in healthy unwounded animals by day 14 post-wounding. In marked contrast, animals receiving PBS vehicle or free HS extract exhibited persistently elevated or only modestly attenuated systemic inflammatory markers. These findings suggest that the local application of PEG-HS/TiO_2 may exert a beneficial systemic anti-inflammatory effect, presumably through mitigation of the local oxidative and inflammatory drivers that would otherwise sustain a state of chronic low-grade inflammation.

To determine whether this systemic attenuation of inflammation correlated with a favorable shift in the local wound immune microenvironment, we examined the transcriptional expression of key cytokines within wound tissue homogenates. Quantitative PCR analysis (Figure 6C and D) revealed a reciprocal regulation of anti- and pro-inflammatory mediators in the PEG-HS/TiO_2-treated group. Specifically, transcript levels of the anti-inflammatory cytokine IL-10 were significantly upregulated (Figure 6C), while expression of the prototypical pro-inflammatory cytokine IL-1β was substantially suppressed (Figure 6D) relative to PBS-treated controls. This cytokine profile is highly suggestive of a resolving, tissue-reparative immunological milieu, aligning closely with the M2-skewed macrophage polarization observed in our in vitro studies (Section 3.4).

To directly visualize the in situ macrophage phenotype within the wound bed, immunofluorescence staining for CD86 (M1 marker) was performed on tissue sections harvested at day 7—a time point corresponding to the transition between the inflammatory and proliferative phases of healing. Representative CLSM images (Figure 6E) depicted abundant CD86-positive cells in the wound beds of PBS-treated animals, indicative of a persistent M1-dominant inflammatory infiltrate. In striking contrast, wounds receiving PEG-HS/TiO_2 exhibited a notable paucity of CD86 immunoreactivity. Quantitative image analysis (Figure 6F) corroborated this visual impression, demonstrating a significant reduction in the CD86-positive area fraction in the nanocomposite-treated group. This in vivo evidence strongly supports the notion that PEG-HS/TiO_2 effectively restrains M1 macrophage persistence within the wound microenvironment, thereby facilitating the timely resolution of inflammation that is requisite for physiological tissue repair.

The ultimate measure of wound healing success extends beyond the rate of closure to encompass the structural and functional integrity of the regenerated tissue. Masson's trichrome staining was therefore employed at day 28 to assess collagen deposition and organization within the remodeled dermis. Representative histological sections (Figure 6G) revealed striking disparities in the quality of the healed tissue across treatment cohorts. Wounds treated with PBS or free HS exhibited collagen fibers that appeared relatively disorganized, with a loose and haphazard arrangement reminiscent of fibrotic or immature scar tissue. Conversely, PEG-HS/TiO_2-treated wounds displayed a denser, more organized collagen network, with fiber bundles approximating the basket-weave orientation characteristic of healthy, unwounded dermis. Immunohistochemical visualization of type I and type III collagen (COL I/COL III) further revealed a more balanced ratio of these two collagen subtypes in the nanocomposite-treated group (Figure 6G, lower panels). Quantitative assessment of collagen volume fraction (Figure 6H) confirmed a significant increase in total collagen content in the PEG-HS/TiO_2 cohort relative to controls. Fluorescence intensity quantification corresponding to COL I and COL III immunostaining (Figure 6K and L) substantiated the qualitative observation of improved collagen architecture, with the COL I/COL III ratio in PEG-HS/TiO_2-treated wounds more closely resembling that of native dermis. These histological findings collectively indicate that PEG-HS/TiO_2 not only accelerates wound closure but also promotes superior regenerative healing, characterized by enhanced collagen maturation and improved matrix organization.

Functional tissue perfusion is an essential determinant of long-term wound stability and resistance to re-injury. Laser speckle contrast imaging (LSCI) was utilized on day 28 to non-invasively assess regional blood perfusion dynamics within the healed wound area. As illustrated in Figure 6I, PEG-HS/TiO_2-treated wounds exhibited markedly enhanced perfusion signals compared to control groups, which displayed relatively attenuated and heterogeneous flow patterns. Quantitative analysis of perfusion units (Figure 6J) revealed a robust and statistically significant increase in blood flow within the regenerated tissue of nanocomposite-treated animals. This sustained improvement in tissue perfusion is likely attributable to the combination of enhanced neovascularization during the proliferative phase (as documented in Figure 5) and the favorable remodeling of the extracellular matrix, which together support the establishment of a stable, functional microvascular network.

The data presented in this section provide a comprehensive portrait of the multifaceted benefits conferred by PEG-HS/TiO_2 in the setting of diabetic wound healing. Beyond the acceleration of gross wound closure, the nanocomposite appears to orchestrate a coordinated series of events that culminate in improved wound prognosis. The attenuation of systemic inflammatory markers (CRP and PCT) suggests that local control of oxidative and inflammatory stress may have beneficial repercussions beyond the wound site itself. Furthermore, the in vivo confirmation of suppressed M1 macrophage persistence and reciprocal regulation of IL-1β and IL-10 lends strong credence to the hypothesis that PEG-HS/TiO_2 functions as an effective local immunomodulator. The histological and functional improvements observed at the late remodeling stage—namely, organized collagen architecture and robust tissue perfusion—underscore the importance of early intervention in the inflammatory cascade for achieving long-term regenerative success. While these findings are highly encouraging, it should be acknowledged that the diabetic mouse model, although widely employed, does not fully recapitulate the complexity of human chronic wounds, which are often complicated by polymicrobial biofilm infections and severe peripheral arterial disease. Future studies may be directed toward evaluating the efficacy of PEG-HS/TiO_2 in large animal models or in combination with standard-of-care debridement and antimicrobial therapies to further establish its translational potential.

Limitations and Future Directions

A limitation of our release study is the use of 37 °C rather than the physiologically relevant skin surface temperature (32–34 °C). While 37 °C facilitates comparison with the broader literature, the actual release kinetics in vivo may differ. Future studies should include release experiments at skin temperature and, ideally, ex vivo skin models to better predict in vivo performance. The diabetic mouse model does not fully recapitulate human chronic wounds, which are often complicated by biofilm infections and peripheral arterial disease. Future studies in large animal models, comprehensive long-term safety assessments, and exploration of antimicrobial combinations may further establish translational potential.

Conclusion

Chronic diabetic wounds are characterized by a self-perpetuating cycle of oxidative stress, persistent inflammation, and impaired neovascularization. To address these interconnected pathologies, we developed PEG-HS/TiO_2, a biomimetic nanocomposite integrating the SOD- and CAT-mimetic activities of mesoporous anatase TiO_2 with the sustained-release bioactivity of honeysuckle (HS)-derived phytochemicals. Physicochemical characterization confirmed a well-defined mesoporous architecture, favorable aqueous dispersibility, and a sustained HS release profile exceeding 72 hours. In vitro, PEG-HS/TiO_2 exhibited potent dual-enzyme mimetic activity, effectively scavenging superoxide anions and hydrogen peroxide. This ROS-neutralizing capacity attenuated cytosolic and mitochondrial oxidative stress in endothelial cells, suppressed senescence markers (SA-β-Gal, p21), and restored VEGF transcription. Concurrently, the nanocomposite redirected macrophage polarization from a pro-inflammatory M1 toward a pro-regenerative M2 phenotype, an effect mechanistically associated with the normalization of H_2O_2-driven glycolytic flux and preservation of mitochondrial spare respiratory capacity. Our supplementary data in Figure S5 (Supporting Information; immunofluorescence and qPCR) suggest that this effect may be mediated, at least in part, through redox-sensitive HIF-1α signaling, although further studies (eg., HIF-1α knockdown or pharmacological inhibition) are warranted to establish causality. In a diabetic murine excisional wound model, topical PEG-HS/TiO_2 accelerated wound closure, enhanced granulation tissue formation, and augmented CD31-positive neovascularization. Local immunomodulation was evidenced by reduced M1 macrophage persistence, diminished IL-1β expression, and elevated IL-10 levels, accompanied by attenuated systemic inflammatory markers (CRP, PCT). Long-term remodeling was characterized by organized collagen architecture, an improved COL I/COL III ratio, and sustained functional tissue perfusion. Collectively, these findings indicate that PEG-HS/TiO_2 disrupts the pathological cycle of diabetic wounds through direct ROS neutralization, alleviation of cellular senescence, and immunometabolic reprogramming of macrophages. By restoring redox homeostasis and promoting a pro-resolving immune phenotype, the nanocomposite accelerates the transition to the proliferative phase and improves regenerative tissue quality. The primary innovation of this study lies in the design of a biomimetic nanocomposite, PEG-HS/TiO_2, that integrates the dual SOD/CAT-mimetic activity of mesoporous anatase TiO_2 with sustained-release honeysuckle phytochemicals to concurrently address three interconnected pathological hallmarks of diabetic wounds: oxidative stress, M1-

dominant inflammation, and endothelial senescence. Unlike conventional approaches that target only one aspect of wound pathology, our nanocomposite orchestrates a coordinated therapeutic cascade—ROS scavenging → HIF-1α destabilization → glycolytic normalization → M2 polarization → angiogenesis → tissue remodeling—thereby breaking the self-perpetuating cycle of chronic inflammation and impaired healing. To our knowledge, this is the first study to demonstrate that a TiO_2-based nanozyme combined with natural phytochemicals can reprogram macrophage immunometabolism via HIF-1α-mediated glycolytic regulation, providing a previously unexplored strategy for diabetic wound management.

Ethics Approval and Consent to Participate

All animal experiments were conducted in strict accordance with the guidelines approved by the Animal Research Ethics Committee of Southern Medical University (experimental Program no. NFYY-2025-0203). The study protocol followed the National Institutes of Health Guide for the Care and Use of Laboratory Animals, and all euthanasia procedures were performed in accordance with the American Veterinary Medical Association (AVMA) Guidelines for the Euthanasia of Animals (https://www.avma.org/resources-tools/avma-policies/avma-guidelines-euthanasia-animals). All methods are reported in accordance with ARRIVE guidelines.

Funding

This research was supported, in whole by Presidential Foundation of the Nanfang Hospital, Southern Medical University (Grant No. 2025B030).

Disclosure

The authors declare no competing interests. All authors have provided consent for the manuscript to be published.

References

1. Chen Y, Wang X, Tao S, et al. Research advances in smart responsive-hydrogel dressings with potential clinical diabetic wound healing properties. *Military Med Res*. 2023;10(1):37. doi:10.1186/s40779-023-00473-9
2. Wilkinson HN, Hardman MJ. Wound healing: cellular mechanisms and pathological outcomes. *Open Biol*. 2020;10(9):200223. doi:10.1098/rsob.200223
3. Seth I, Gibson D, Lim B, et al. Advancements, applications, and safety of negative pressure wound therapy: a comprehensive review of its impact on wound outcomes. *Plastic Aesthetic Res*. 2024;11:29.
4. Aitcheson SM, Frentiu FD, Hurn SE, Edwards K, Murray RZ. Skin wound healing: normal macrophage function and macrophage dysfunction in diabetic wounds. *Molecules*. 2021;26(16):4917. doi:10.3390/molecules26164917
5. Huang F, Lu X, Yang Y, et al. Microenvironment-based diabetic foot ulcer nanomedicine. *Adv Sci*. 2023;10(2):e2203308. doi:10.1002/advs.202203308
6. Roehrs H, Stocco JG, Pott F, Blanc G, Meier MJ, Dias FA. Dressings and topical agents containing hyaluronic acid for chronic wound healing. *Cochrane Database Systematic Rev*. 2023;7(7):Cd012215. doi:10.1002/14651858.CD012215.pub2
7. Kang Q, Yang C. Oxidative stress and diabetic retinopathy: molecular mechanisms, pathogenetic role and therapeutic implications. *Redox Biol*. 2020;37:101799. doi:10.1016/j.redox.2020.101799
8. Du D, Liu C, Qin M, et al. Metabolic dysregulation and emerging therapeutical targets for hepatocellular carcinoma. *Acta pharmaceutica Sinica B*. 2022;12(2):558–580.
9. Averill-Bates D. Reactive oxygen species and cell signaling. Review, biochimica et biophysica acta. *Molecular Cell Res*. 2024;1871(2):119573. doi:10.1016/j.bbamcr.2023.119573
10. Liu D, Qin H, Gao Y, Sun M, Wang M. Cardiovascular disease: mitochondrial dynamics and mitophagy crosstalk mechanisms with novel programmed cell death and macrophage polarisation. *Pharmacolog Res*. 2024;206:107258. doi:10.1016/j.phrs.2024.107258
11. Deng ZH, Yang ZL, Yi S, Liu ZQ. Hydrogel-exosome systems in the treatment of refractory diabetic ulcers: mechanisms, progress, and prospects. *Eur Cell Mater*. 2025;53:82–97. doi:10.22203/eCM.v053a07
12. Zhang Q, Liu J, Duan H, Li R, Peng W, Wu C. Activation of Nrf2/HO-1 signaling: an important molecular mechanism of herbal medicine in the treatment of atherosclerosis via the protection of vascular endothelial cells from oxidative stress. *J Adv Res*. 2021;34:43–63. doi:10.1016/j.jare.2021.06.023
13. An Y, Xu BT, Wan SR, et al. The role of oxidative stress in diabetes mellitus-induced vascular endothelial dysfunction. *Cardiovascu Diabetol*. 2023;22(1):237. doi:10.1186/s12933-023-01965-7
14. He S, Li Z, Huang W, et al. Functional phyto-nanozymes for dual regulation of microbial metabolism and overinflammation microenvironment in diabetic wound. *Materials Today Bio*. 2025;35:102293. doi:10.1016/j.mtbio.2025.102293
15. Shen J, Pan Y, Han L, Luo L, Sun T, Yu Y. Nanozymes as next-generation ROS scavengers: design strategies, catalytic mechanisms, and therapeutic frontiers. *J Mater Chem*. 2025;13(28):8286–8297. doi:10.1039/D5TB00849B
16. Xu D, Wu L, Yao H, Zhao L. Catalase-like nanozymes: classification, catalytic mechanisms, and their applications. Small. 2022;18(37):e2203400.

17. Qi J, Liu H, Li H, et al. How TiO(2) nanomaterials are emerging as key therapeutics in stomatology. *Int J Nanomed*. 2025;20:11451–11478. doi:10.2147/IJN.S533650
18. Ścibior A, Pietrzyk Ł, Plewa Z, Skiba A. Vanadium: risks and possible benefits in the light of a comprehensive overview of its pharmacotoxicological mechanisms and multi-applications with a summary of further research trends. *J Trace Elements Med Biol*. 2020;61:126508. doi:10.1016/j.jtemb.2020.126508
19. Zhang X, Li W, Yang Z. Toxicology of nanosized titanium dioxide: an update. *Archives of Toxicology*. 2015;89(12):2207–2217. doi:10.1007/s00204-015-1594-6
20. Yang Z, Shi L, Wang Y, Zhou D, Zhang C, Lin Y. Unveiling the potential of tetrahedral DNA frameworks in clinical medicine: mechanisms, advances, and future perspectives. *Small*. 2025;21(5):2410162.
21. Inada Y, Furukawa M, Sasaki H, et al. Biomedical and biotechnological applications of PEG- and PM-modified proteins. *Trends Biotechnol*. 1995;13(3):86–91. doi:10.1016/S0167-7799(00)88912-X
22. Arkas M, Vardavoulias M, Kythreoti G, Giannakoudakis DA. Dendritic polymers in tissue engineering: contributions of PAMAM, PPI PEG and PEI to injury restoration and bioactive scaffold evolution. *Pharmaceutics*. 2023;15(2).
23. He S, Li Z, Wang L, et al. A nanoenzyme-modified hydrogel targets macrophage reprogramming-angiogenesis crosstalk to boost diabetic wound repair. *Bioact Mater*. 2024;35:17–30. doi:10.1016/j.bioactmat.2024.01.005
24. Ngungeni Y, J AA, Moabelo KL, et al. Anticancer, antioxidant, and catalytic activities of green synthesized gold nanoparticles using avocado seed aqueous extract. *ACS Omega*. 2023;8(29):26088–26101. doi:10.1021/acsomega.3c02260
25. Gao S, Shan Y, Wang Y, Wang W, Li J, Tan H. Polysaccharides from lonicera japonica thunb: extraction, purification, structural features and biological activities-A review. *Int J Biol Macromol*. 2024;281(Pt 4):136472. doi:10.1016/j.ijbiomac.2024.136472
26. Bai X, Liu P, Shen H, Zhang Q, Zhang T, Jin X. Water-extracted Lonicera japonica polysaccharide attenuates allergic rhinitis by regulating NLRP3-IL-17 signaling axis. *Carbohydr Polym*. 2022;297:120053. doi:10.1016/j.carbpol.2022.120053
27. Shang X, Pan H, Li M, Miao X, Ding H. Lonicera japonica Thunb.: ethnopharmacology, phytochemistry and pharmacology of an important traditional Chinese medicine. *J Ethnopharmacol*. 2011;138(1):1–21. doi:10.1016/j.jep.2011.08.016
28. Zhang Y, Cao Y, Zhang X, et al. Single-cell RNA sequencing uncovers pathological processes and crucial targets for vascular endothelial injury in diabetic hearts. *Adv Sci*. 2024;11(47):e2405543. doi:10.1002/advs.202405543
29. Almalki WH, Almujri SS, Aging. ROS, and cellular senescence: a trilogy in the progression of liver fibrosis. *Biogerontology*. 2024;26(1):10. doi:10.1007/s10522-024-10153-3
30. Picos A, Seoane N, Campos-Toimil M, Viña D. Vascular senescence and aging: mechanisms, clinical implications, and therapeutic prospects. *Biogerontology*. 2025;26(3):118. doi:10.1007/s10522-025-10256-5
31. Zhang QY, Zhang HY, Feng SG, et al. Macrophage metabolic reprogramming ameliorates diabetes-induced microvascular dysfunction. *Redox Biol*. 2025;79:103449. doi:10.1016/j.redox.2024.103449